Ocean Modelling 89 (2015) 1–28

Contents lists available at ScienceDirect

Ocean Modelling

journal homepage: www.elsevier.com/locate/ocemod

Optimizing velocities and transports for complex coastal regions and archipelagos

Patrick J. Haley Jr. *, Arpit Agarwal, Pierre F.J. Lermusiaux

Massachusetts Institute of Technology, Cambridge, MA 02139, USA

ARTICLE INFO

Article history:
Received 10 November 2013
Received in revised form 5 February 2015
Accepted 22 February 2015
Available online 6 March 2015

Keywords:
Fast Marching Method
Downscaling
Two-way nesting
Primitive-equation
Euler–Lagrange
Reduced-dynamics

ABSTRACT

We derive and apply a methodology for the initialization of velocity and transport fields in complex multiply-connected regions with multiscale dynamics. The result is initial fields that are consistent with observations, complex geometry and dynamics, and that can simulate the evolution of ocean processes without large spurious initial transients. A class of constrained weighted least squares optimizations is defined to best fit first-guess velocities while satisfying the complex bathymetry, coastline and divergence strong constraints. A weak constraint towards the minimum inter-island transports that are in accord with the first-guess velocities provides important velocity corrections in complex archipelagos. In the optimization weights, the minimum distance and vertical area between pairs of coasts are computed using a Fast Marching Method. Additional information on velocity and transports are included as strong or weak constraints. We apply our methodology around the Hawaiian islands of Kauai/Niihau, in the Taiwan/Kuroshio region and in the Philippines Archipelago. Comparisons with other common initialization strategies, among hindcasts from these initial conditions (ICs), and with independent *in situ* observations show that our optimization corrects transports, satisfies boundary conditions and redirects currents. Differences between the hindcasts from these different ICs are found to grow for at least 2–3 weeks. When compared to independent *in situ* observations, simulations from our optimized ICs are shown to have the smallest errors.

1. Introduction

Imagine that the Lorenz-63 system (Lorenz, 1963) was representative of the real ocean. Imagine that your goal was to initialize a useful prediction for this system, from imperfect measurements. By useful prediction, we mean the capability of predicting for some time, in the ideal case up to the local predictability limit (initial-condition-dependent). If you knew that the initial state was not zero, why would you spin-up from zero? If one of the state variables was measured initially, but with uncertainty, someone may guess an initial condition by running the Lorenz model for some time, keeping the measured state variable fixed. Unless that person is so lucky to stop at the right time, the likelihood of the result being close to the true initial condition is very small. Hence, being on the "attractor" of the model is not enough. What we need is to be in a neighborhood of the true initial state, such that if we start a prediction from that state, some predictive capability exists. We remark that in that case, the subsequent assimilation of limited data will also have a much easier time at controlling error growth. And second, if the model was imperfect, running the model for too long in the initial adjustment may also lead to large errors. The present manuscript is concerned with such estimation of initial ocean conditions, focusing on regions with complex geometries and multiscale dynamics governed by hydrostatic primitive equations (PEs) (e.g. Cushman-Roisin and Beckers, 2010) with a free ocean surface, referred to next simply as free-surface PEs (e.g. Haley and Lermusiaux, 2010, hereafter denoted as HL10).

The estimation of initial conditions (ICs) for ocean simulations is not a new problem (Wunsch, 1996). For longer time-scale prediction (e.g. climatological studies) the use of spin-up from rest to initialize simulations has been frequent (Artale et al., 2010; Maslowski et al., 2004; Schiller et al., 2008; Timmermann et al., 2005; Zhang and Steele, 2007) in part because of lack of data for initialization. Even for shorter time-scale predictions with more synoptic information, spin-up from rest is still often used. However, studies show that using ICs which are not in dynamical balance (e.g. the zero velocities at the start of the spin-up from rest) can lead to numerical shock (Oke et al., 2002) and erroneous

* Corresponding author.
E-mail addresses: phaley@mit.edu (P.J. Haley Jr.), arpit@mit.edu (A. Agarwal), pierrel@mit.edu (P.F.J. Lermusiaux).

http://dx.doi.org/10.1016/j.ocemod.2015.02.005
1463-5003/

dynamics (Robinson, 1996, 1999; Lozano et al., 1996; Beşiktepe et al., 2003). Some variations on the spin-up procedure have been used to control shocks, including: multi-stage spin-up schemes (Cazes-Boezio et al., 2008; Jiang et al., 2009); spin-up with data assimilation (Balmaseda et al., 2008; Balmaseda and Anderson, 2009; Bender and Ginis, 2000; Cazes-Boezio et al., 2008); and spin-up with relaxation to a reference field (Halliwell et al., 2008; Sandery et al., 2011). Other methods to incorporate more synoptic scales and dynamics into the initial fields include feature models (FM; Gangopadhyay et al., 2003, 2011, 2013; Schmidt and Gangopadhyay, 2013; Falkovich et al., 2005; Yablonsky and Ginis, 2008) and downscaling (Pinardi et al., 2003; Barth et al., 2008; Mason et al., 2010; Halliwell et al., 2011; Herzfeld and Andrewartha, 2012). Studies of ocean responses to atmospheric forcing also highlighted the need of incorporating synoptic scales and dynamics from the beginning (Falkovich et al., 2005; Halliwell et al., 2008, 2011). Here we incorporate the synoptic scales and dynamics by creating dynamically balanced initializations for *multiply-connected domains*.

Our approach is to efficiently estimate three-dimensional (3D) initial velocity fields that are consistent with the synoptic observations available, complex geometry, free-surface PEs and any other relevant information by defining and semi-analytically solving a global constrained optimization problem. By consistent initial velocity fields, we signify fields that would evolve in accord with the free-surface PE dynamics in the complex region, simulating the evolution of these ocean processes without spurious initial transients. By "semi-analytically", we mean that we analytically derive the Euler–Lagrange equations that optimize the cost function and then solve these equations numerically. Our approach is in contrast with procedures that attempt to build flows from scratch solely through model dynamical adjustment, i.e. through time-integration of a numerical model. However, our aim is not to replace the estimation of ICs by weak- or strong-constraint generalized inversions over time (Bennett, 1992; Bennett, 2002; Moore, 1991; Moore et al., 2004, 2011). Instead, it is to compute consistent ICs. They can then lead to useful predictions or be employed as starting conditions in a generalized inversion.

Some key technical questions arise due to the complex geometries and multiscale flows. They include: how to account for multiple islands, tortuous coastlines and variable bathymetries, respecting boundary conditions? how to compute the minimum vertical ocean area between islands? how to utilize these areas to set through-flows or local currents within (or near) expected values? how to optimize the kinetic energy locally, eliminating unrealistic hot-spots? how to ensure conservative 3D flow fields that satisfy continuity constraints with a free ocean surface? and finally, how to respect a sufficiently accurate internal dynamics in accord with the observations available and the scales being modeled? To address such questions, we introduce a subtidal/tidal separation of velocities and obtain first-guess subtidal velocity fields from reduced dynamics and hydrographic and flow data. Our optimization then best-fits these first-guess subtidal velocity fields, enforcing tortuous coastline, bathymetry and divergence strong constraints. To enforce all of these constraints, cost functions are defined and Euler–Lagrange equations that optimize these cost functions are derived and numerically solved. Novel elements of this methodology include: the incorporation of weighting functions in the cost functions; derivation of the optimal Dirichlet open boundary conditions (OBCs); and the optimization of the inter-island transports and near island flows, which provides important velocity corrections in complex archipelagos. To set the weights for the horizontal streamfunctions along island coastlines, the minimum distance and vertical area between pairs of islands are computed using a Fast Marching Method (FMM; Sethian, 1996, 1999). The use of all available information to optimally estimate the inter-island transports makes our methodology a generalization of the "island rule" (Godfrey, 1989). Our methodology can also incorporate estimates from the "island rule" as weak constraints.

Problem statement and rationale. Mathematically, denoting the PE state variable fields as: temperature T; salinity S; horizontal and vertical components of velocity $\vec{u}$ and w; and free-surface elevation η, our objective is to: (i) obtain initial fields that optimize a constrained cost function J in a complex domain, $\mathcal{D}$, with boundary $\partial\mathcal{D}$ (open boundaries and coastlines) i.e.,

$$\arg\min_{[\vec{u},w,\eta,T,S]} J(\text{data, complex geometry, dynamics}) \quad \text{in} \quad \mathcal{D}\cup\partial\mathcal{D};$$

but also (ii) determine such a cost function J and corresponding direct solution scheme that will efficiently compute consistent initial velocity fields.

Of course, there are uncertainties even in the form of the cost function, the constraints and their parameters (Lermusiaux, 2007). We thus seek to respect the synoptic data, complex geometry, scales and dynamics (or representative reduced dynamics) only within uncertainties. In other words, the objective is to derive an efficient scheme that computes ICs close enough to the ocean state at the initial time, so as to subsequently evolve without spurious transients due to complex bathymetry and islands (geometry), and also without the possible assimilation shocks. As a result, we aim to avoid creating initial velocities solely via a model "dynamical adjustment" from too inaccurate first-guesses (e.g. either too large or too small velocities, as in the extreme case of a model "spin-up" from zero velocities). To illustrate issues with such adjustments, consider first the case where T/S remain fixed while $\vec{u}$, w and η are adjusted from a too inaccurate first-guess. Model errors (discretization and other error modes) can grow in the velocity fields during the adjustment. Also, due to nonlinear terms in the free-surface PEs, even if the T/S fields are perfect, the velocity adjustment may either not converge or converge but not towards the true velocity everywhere in the complex domain. Second, if a first-guess velocity far from the truth is instead adjusted by allowing T and S to vary during the adjustment, then potential energy and kinetic energy would be inter-changed. The resulting adjusted density and velocity fields would differ from the true ones, e.g. be in a different energy balance or "attractor regime" than the real one. Critically, such adjusted fields retain some memory of the too erroneous first-guess velocity. Model predictions from these fields would then be damaged for some time. All of these considerations due to complex geometries are exemplified in Sections 4.1 and 4.2. Only data assimilation (DA), i.e. re-initialization, could correct these biases.

In what follows, we present our methodology for ICs in complex domains (Section 2). In Section 3, we derive the core algorithms to optimally fit velocities and transports (Section 3.1) and to optimize them between and near islands (Section 3.2). In Section 4, we apply our methodology around the Hawaiian islands of Kauai/Niihau (Section 4.1), in the Taiwan/Kuroshio region (Section 4.2) and in the Philippines Archipelago (Section 4.3). Quantitative comparisons (i) with other commonly-used initialization strategies, (ii) among hindcasts from these ICs and (iii) with independent *in situ* observations, show that our complex-domain optimization corrects velocity estimates and incorporates critical constraints on the net transports, all of which lead to more accurate forecasts in multiply-connected regions. These are coastal mesoscale examples but our methodology is applicable to other scales. A summary and conclusions are in Section 5. The free-surface PEs and our modeling system are outlined in Appendix A. Specifics of the methodology, including some details of the derivations, are in Appendices B–D.

2. Methodology: overall scheme

In this section we present a high-level description of our methodology for constructing PE-balanced initialization fields in complex domains, including nesting and downscaling. The steps are outlined in Sections 2.1–2.3 and summarized in Table 1. Implicit in these steps is a separation of the subtidal and tidal velocities/transports (Section 2.3). These steps provide the context within which we derive our core algorithms of Section 3 for the subtidal velocities/transports. These core algorithms solve a weighted least squares optimization by obtaining the exact solutions to Euler–Lagrange equations for streamfunction formulations of subtidal velocity/transport. The specific equations solved are: (i) a 1D Poisson equation along the external boundary for the Dirichlet OBCs, (ii) algebraic equations for the constant values for the streamfunction along the uncertain islands which optimize the inter-island transports and near-island flows and (iii) a Poisson equation for the streamfunction, using the BCs from (i) and (ii). Since we focus on velocity optimization, we omit a discussion on input data, models, etc., which we provide in Haley et al., 2014.

2.1. First-guess velocity

We start by estimating first-guess velocity fields, $\vec{u}_{(0)}$ and $w_{(0)}$, that are in dynamical balance among each other and with the T/S fields, represent the specific scales of interest, and satisfy simple bathymetric constraints. These $\vec{u}_{(0)}$ and $w_{(0)}$ are the starting point for adding more complicated coastal, bathymetric and transport constraints. The subscript (n) represents the n^{th}-correction of a quantity, hence $\vec{u}_{(0)}$ is the first guess velocity, $\vec{u}_{(1)}$ is the first correction velocity and so on.

Reduced-dynamics models are often used in conjunction with mapped T/S fields as the starting point for constructing $\vec{u}_{(0)}$ and $w_{(0)}$. A commonly used reduced model is geostrophy, specifically integrating the thermal wind equations (Wunsch, 1996; Marshall and Plumb, 2008; Haley et al., 2014). The $\vec{u}_{(0)}$ and $w_{(0)}$ can also combine: additional dynamics (e.g. Ekman dynamics and other boundary layers); velocity feature models and data (*in situ* and remote). When available, prior knowledge of the flow (e.g. net transports, velocity values or throughflow range) should be used to constrain estimates. All of these combinations should properly account for the uncertainties in the data and estimates. Examples are shown in Section 4.

One can use the velocity fields from existing numerical simulations (often at coarser resolutions). We treat these as first-guess velocities because they usually do not fit all of our dynamics, scales and resolution. One simple constraint we directly impose on $\vec{u}_{(0)}$ is to set the velocities to zero under the model bathymetry (this can require care, see Haley et al., 2014).

2.2. Complex geometry constraints

The first guess velocities $\vec{u}_{(0)}$ do not respect all model geometry constraints nor the bottom-related dynamics. Geostrophic velocities rarely satisfy no-normal flow through coastlines and bottom balances. Velocities obtained from other simulations are in balance with their own bathymetry and coasts, which, in our applications, are usually of coarser resolution. Reduced dynamics models and feature models may or may not take either bathymetry or coasts into account. Therefore the next step in our scheme is to adjust the first guess velocities to the modeled bathymetry and coasts.

Coastal constraints. We first discuss imposing constraints on $\vec{u}_{(0)}$ defined on constant-depth levels (which can then be interpolated to other vertical coordinates). No-normal flow into coasts is imposed on levels which reach the coasts in water and on any

Table 1
Summary of the six steps of our scheme to initialize velocity and transport for PE simulations in complex geometries (multiply-connected domains). Table is presented in the order the operations are performed. Repeat steps 1–6 for nested sub-domains.

(1) Input data and models for computing velocity	
(2) (Section 2.1) Compute first-guess velocity $\vec{u}_{(0)}$	
• Use data and reduced models to estimate velocity	e.g. thermal wind
• Enforce direct bathymetry strong constraints, e.g. zero flow below bathymetry, compute consistent $\vec{u}_{(0)}$	
(3) (Section 2.2) Geometry constraints: Best-fit $\vec{u}_{(0)}$ level-by-level, enforcing coastline strong constraints	
• Best fit 3D velocities, enforcing no-normal flow through coastlines.	
◦ Propagate interior data to uncertain BCs (island-free)	Table 2a, Eq. (11)in Section 3.1
◦ Best fit external BCs (interpolate for nesting)(island-free)	Table 2a, Eq. (10) in Section 3.1
◦ Best fit internal island BCs, solving weak-constraint optimization	Table 2a, Eqs. (12) and (15) in Section 3.2
◦ Combine all BCs and best-fit no-normal flow velocity	Table 2a, Eqs. (5) and (16) in Section 3.1
	$\vec{u}_{(1)} = \hat{k} \times \nabla\psi$ Eq. (4)
• To retain 3D effects or more complex bathymetry constraints, solve for corrector velocity	Appendix B
	$\vec{u}_{(2)} = \vec{u}_{(1)} + \nabla\phi$ Eq. (B.16)
• Compute first-guess sub-tidal transports from the resultant geometry-constrained velocity.	$\vec{U}_{(0)} = \begin{cases} \int_{-H}^{0} \vec{u}_{(2)}\, dz & \text{if 3D constraints} \\ \int_{-H}^{0} \vec{u}_{(1)}\, dz & \text{otherwise} \end{cases}$ Eq. (1)
(4) (Section 2.3) Sub-tidal transport strong constraints: best-fit transport in (complex)-domain, enforcing non-divergence	
• Best fit non-divergent transport to $H\vec{U}_{(0)}$ obtained in Section 2.2 and other transport data	
◦ Propagate interior data to uncertain BCs (island-free)	Table 2b, Eq. (1)in Section 3.1
◦ Best fit external BCs (interpolate for nesting)(island-free)	Table 2b, Eq. (10) in Section 3.1
◦ Best fit internal island BCs, solving weak-constraint optimization	Tables 2b, Eqs. (12) and (15) in Section 3.2
◦ Combine all BCs and best-fit non-divergent transport preserving no-normal flow	Table 2b, Eqs. (5) and (16) in Section 3.1
	$H\vec{U}_{(1)} = \hat{k} \times \nabla\Psi$ Eq. (3)
(5) (Section C.1) Solve for sub-tidal free surface $\eta_{(0)}$	e.g., $\eta_{(0)}$ from HL10 Eq. (68)
	$\vec{U}_{(2)} = \frac{H}{H+\eta_{(0)}} \vec{U}_{(1)}$ Eq. (C.1)
(6) (Section C.2) Superimpose tides η_{tide} and $\vec{U}_{tide}$, preserving divergence and no-normal flow strong constraints	$\eta_{(1)} = \eta_{(0)} + \eta_{tide}$ Eq. (C.2)
	$\vec{U}_{(3)}$ from Eq. (C.3)
	$\vec{u}'$ from Eq. (C.4)
	$\vec{u} = \vec{u}' + \vec{U}_{(3)}$ Eq. (C.5)
	$w = -\int_{-H}^{z} \nabla \cdot \vec{u}\, d\zeta - (\vec{u} \cdot \nabla H)\vert_{z=-H}$ Eq. (C.6)

additional levels used in subsequent interpolations. For all levels below these, no additional constraints are enforced.

The method to enforce no-normal flow into coastlines employs a constrained least squares minimization to find the first correction velocity, $\vec{u}_{(1)}$, which at all depths/levels best fits the first-guess, $\vec{u}_{(0)}$, while satisfying $\vec{u}_{(1)} \cdot \hat{n}\big|_{\partial\mathcal{D}} = 0$. This optimum is obtained by solving 2D elliptical problems exactly in one iteration. The algorithm is derived later in Sections 3 to allow for a unified presentation of both the flow and transport constraints.

For terrain-following vertical coordinates, the no-normal flow constraint is imposed on velocities at constant-depth levels and the results are interpolated to terrain-following. For isopycnal or generalized coordinates (HL10), the situation is similar to the constant-depth vertical coordinates and the optimization is applied for layers/levels reaching the coasts.

Below the levels where we impose no-normal flow into coasts, we could use the above optimization to force the very bottom flows to be aligned with isobaths. However, this is only done when we have strong physical evidence for such isobaths-aligned bottom flows (see Haley et al., 2014).

3D effects and more complicated bathymetry constraints. When the full 3D flow dynamics is critical, we update the algorithm outlined above into a 3D (x,y,z) best fit. One example is the initialization from an existing numerical simulation (i.e. downscaling). These fields are in their own 3D dynamical balance and are assumed to be sufficiently resolved to contain a useful $w_{(0)}$ at the new, refined, resolution. The goal is then to maintain as much of this 3D balance as is consistent with the model being initialized. Other examples (see Haley et al., 2014) involve the use of 3D feature models or reduced 3D dynamics (e.g. geostrophy and Ekman forcing). In Appendix B, we derive a predictor–corrector algorithm for fitting the no-normal flow constraints in 3D, including vertical velocity w information. The result of this algorithm is the second correction velocity, $\vec{u}_{(2)} = \vec{u}_{(1)} + \Delta\vec{u}$, that recovers the first guess vertical velocity by imposing the constraint $\nabla \cdot \vec{u}_{(2)} \approx -\frac{\partial w_{(0)}}{\partial z}$, where $\nabla\cdot$ is the horizontal divergence operator. Without this correction, the streamfunction formulation loses the information on w.

First-guess sub-tidal transport. Once the geometry-constrained $\vec{u}_{(1)}$ (or $\vec{u}_{(2)}$) is computed, it is used to obtain the first-guess transport, $H\vec{U}_{(0)}$, from either

$$H\vec{U}_{(0)} = \begin{cases} \int_{-H}^{0} \vec{u}_{(2)}\, dz & \text{if 3D constraints (see Appendix B)} \\ \text{or } \int_{-H}^{0} \vec{u}_{(1)}\, dz & \text{otherwise} \end{cases} \tag{1}$$

where $\vec{U}$ is the local total-depth-averaged velocity and $H(x,y)$ the local total depth of the water column. In Section 2.3 our optimization starts from $H\vec{U}_{(0)}$ over $\mathcal{D}$ and imposes additional (strong) transport constraints, leading to the first correction transport estimate, $H\vec{U}_{(1)}$ over $\mathcal{D}$.

2.3. Sub-tidal transport constraints

The final constraint on velocity in complex domains is applied on the divergence of the horizontal transport. From Eq. (A.7), this $\nabla \cdot (H\vec{U})$ is directly related to $\frac{\partial\eta}{\partial t}$. We consider separately the portions of the transport with significant contributions to $\frac{\partial\eta}{\partial t}$ and those with negligible contributions.

This rate $\frac{\partial\eta}{\partial t}$ is a function of both external processes (tides, evaporation – precipitation, rivers, open boundaries) and local processes (e.g. density driven flows). Generally only tides produce significant contributions to $\frac{\partial\eta}{\partial t}$ (i.e. barring floods and other catastrophic events, the remaining processes either have time scales which are too slow or amplitudes which are too small). We compute the portions of the initial transport with negligible contributions to $\frac{\partial\eta}{\partial t}$, i.e. the non-divergent sub-tidal transport, and superimpose tidal elevations and transports from the tidal fields that will force the simulation being initialized. The result is initial and boundary transports with dynamically-balanced divergences. During the construction of the transports, the constraint of no-normal flow into the complex coastlines is re-imposed to ensure that both it and the desired divergence are maintained in the final solution.

A constrained optimization is employed to find the non-divergent sub-tidal transport, $H\vec{U}_{(1)}$, that best fits $H\vec{U}_{(0)}$ subject to the constraints of no-normal flow at the complex coasts, i.e. $\vec{U} \cdot \hat{n}\big|_{\partial\mathcal{D}} = 0$, and of non-divergence, i.e. $\nabla \cdot \left(H\vec{U}_{(1)}\right) = 0$. This procedure, essentially the same as that for imposing no-normal flow on the velocities, ensures that the final 3D velocities will maintain no-normal flow into coasts and is derived in Section 3.

Free surface and tidal initialization. The final steps in the algorithm ensure the consistency amongst the initial transports, initial free surface and tidal forcing. This material was largely presented in HL10 and is summarized in Appendix C in the notation of the present manuscript.

3. Methodology: core algorithms

We now derive the core algorithms for our constrained optimization of the initial velocities and transports in complex domains. Our semi-analytical methodology (summarized in Table 2) starts by a global weighted optimization of the open boundary values to the first guess and geometric and divergence constraints, in the absence of islands. We employ these optimized values and certain island conditions in a best fit of velocities and transports (subject to the same constraints). From this solution, we obtain initial estimates for minimum transports between each island and all other coasts. With these estimates and the best-fit OBC values, we solve our constrained weighted optimization of the initial velocities and transports in the presence of islands. Weighting functions are defined using uncertainty and physics considerations. To obtain the exact solutions for these best fits, we derive successive Euler–Lagrange equations for the interior, boundary and island streamfunctions. This is done next for the case of fitting transports, adding notes when needed for fitting 3D velocities.

3.1. Core algorithm to optimize sub-tidal transports and velocities

The algorithm employs a least squares minimization to find the sub-tidal $H\vec{U}_{(1)}$ that best fits the first guess $H\vec{U}_{(0)}$ (Eq. 1) under the geometric and divergence constraints with a specific focus on no-normal flow in complex geometries. To obtain the exact solutions for these optimizations, we derive (i) a Poisson equation (Eq. (5)) in $\mathcal{D}$ for a streamfunction representation of the transport or velocity, i.e. Ψ for $H\vec{U}_{(1)}$ or ψ for $\vec{u}_{(1)}$ and (ii) a 1D Poisson equation (Eq. (10)) along the external boundary, $\partial\mathcal{D}^e$, for the Dirichlet OBCs, Ψ_{b^e} or ψ_{b^e}, which best fit the flow through the open boundaries. Specifically, the weighted least squares cost function, J, is defined as

$$\begin{aligned} J(\vec{\tilde{H}}_{(1)}) &= \frac{1}{2}\iint_{\mathcal{D}} \omega \left\| H\vec{U}_{(0)} - \vec{\tilde{H}}_{(1)} \right\|^2 da \\ \text{subject to } \nabla \cdot (\vec{\tilde{H}}_{(1)}) &= 0 \quad \text{(non-divergence)}, \\ \vec{\tilde{U}}_{(1)} \cdot \hat{n}\Big|_{\partial\mathcal{D}} &= 0 \quad \text{(no-normal flow into coasts)}, \end{aligned} \tag{2}$$

Table 2
Summary of algorithm (Section 3) for computing the: (a) 3D velocity (level-by-level $\vec{u}$ and then w from Eq. (C.6)); and (b) transport. Both are optimized for domains with complex geometries including islands. Intermediate transports/velocities can be computed from the intermediate streamfunctions, but are not needed for the algorithm.

(a) Algorithm for 3D velocity	
Propagate interior data to boundaries (Eq. (11)) • in 2nd BC, $\partial^2\psi_{(-1)}/\partial n\partial t$ is a simple weak OBC, conserving the normal advective flux (locally maintained streamfunction). Other good choices are possible • (11) not needed for downscaling or "certain boundaries"	$\nabla\cdot\left(\omega\nabla\psi_{(-1)}\right)=\left[\nabla\times\left(\omega\vec{u}_{(0)}\right)\right]\cdot\hat{k}$ $\psi_{(-1)}\big\|_{C^{1cst}}=\psi_{C^{1cst}}$ and either $\nabla\psi_{(-1)}\cdot\hat{n}\big\|_{\partial\mathcal{D}}=-\hat{k}\times\vec{u}_{(0)}\cdot\hat{n}\big\|_{\partial\mathcal{D}}$ or zero wt & weak OBC $\omega\|_{\partial\mathcal{D}}=0\quad\&\quad\frac{\partial u\cdot\hat{n}}{\partial n}\big\|_{\partial\mathcal{D}}=\frac{\partial^2\psi_{(-1)}}{\partial n\partial t}\big\|_{\partial\mathcal{D}}=0$
Construct exterior BCs (optimize J_b, Eq. 10) using either original $\vec{u}_{(0)}$ or recomputed $\vec{u}_{(0)}$ above (for nesting, interpolate ψ_{b^e} from larger domain)	recompute : $\vec{u}_{(0)}=\hat{k}\times\nabla\psi_{(-1)}$ $-\frac{\partial}{\partial s}\left(\omega\frac{\partial\psi_{b^e}}{\partial s}\right)=\frac{\partial}{\partial s}\left(\omega\vec{u}_{(0)}\cdot\hat{n}\right)$ along open boundaries $-\left(\omega\frac{\partial\psi_{b^e}}{\partial s}\right)\Big\|_{C_m^{e-}}^{C_m^{e+}}=\left(\omega\vec{u}_{(0)}\cdot\hat{n}\right)\big\|_{C_m^{e-}}^{C_m^{e+}}$ at unknown coasts $\{C_m^e\}$ $\psi_{b^e}\big\|_{C_m^{e-}}^{C_m^{e+}}=0$ at unknown coasts $\{C_m^e\}$ $\psi_{b^e}\big\|_{C_k^e}=\psi_{C_k^e}$ at known coasts $\{C_k^e\}$
Construct "certain coast" solution (Eq. 12) using ψ_{b^e} from above	$\nabla\cdot\left(\omega\nabla\psi_{(0)}\right)=\left[\nabla\times\left(\omega\vec{u}_{(0)}\right)\right]\cdot\hat{k}$ $\psi_{(0)}\big\|_{\partial\mathcal{D}^e}=\psi_{b^e}\equiv\begin{cases}\psi_{b^e} & \text{if } s\in\partial\mathcal{D}^e\\ \psi_{C_k^{ic}} & \text{if } s\in C_k^{ic}\end{cases}$
Construct interior island BCs (optimize J_{b^u}, Eq. 15) using $\psi_{(0)}$ from above	$\left[\sum_{m\neq n}^{N^{iu}}\varpi_{nm}^{uu}+\sum_{k=1}^{M^c}\varpi_{nk}^{uc}+\varpi_{nb}^{uo}\right]\psi_{C_n^{iu}}-\sum_{m\neq n}^{N^{iu}}\varpi_{nm}^{uu}\psi_{C_m^{iu}}=\sum_{m\neq n}^{N^{iu}}\varpi_{nm}^{uu}\Delta_{nm}^{uu}\psi_{(0)}+\sum_{k=1}^{M^c}\varpi_{nk}^{uc}\psi_{(0)}(s_{nk}^{uc})+\varpi_{nb}^{uo}\psi_{(0)}(s_{nb}^{uo})$
Solve full problem (optimize J, Eqs. (5) and (16)) using ψ_{b^e} and $\psi_{C_n^{iu}}$ from above	$\nabla\cdot(\omega\nabla\psi)=\left[\nabla\times\left(\omega\vec{u}_{(0)}\right)\right]\cdot\hat{k}$ $\psi\|_{\partial\mathcal{D}}=\psi_b\equiv\begin{cases}\psi_{b^e} & \text{if } s\in\partial\mathcal{D}^e\\ \psi_{C_k^{ic}} & \text{if } s\in C_k^{ic}\\ \psi_{C_n^{iu}} & \text{if } s\in C_n^{iu}\end{cases}$
(b) Algorithm for transport	
Propagate interior data to boundaries (Eq. (11)) • in 2nd BC, $\partial^2\Psi_{(-1)}/\partial n\partial t=0$ is a simple weak OBC, conserving the normal advective flux (locally maintained streamfunction). Other good choices are possible • (11) not needed for downscaling or"certain boundaries"	$\nabla\cdot(\omega\nabla\Psi_{(-1)})=\left[\nabla\times\left(\omega H\vec{U}_{(0)}\right)\right]\cdot\hat{k}$ $\Psi_{(-1)}\big\|_{C^{1cst}}=\Psi_{C^{1cst}}$ and either $\nabla\Psi_{(-1)}\cdot\hat{n}\|_{\partial\mathcal{D}}=-\hat{k}\times H\vec{U}_{(0)}\cdot\hat{n}\big\|_{\partial\mathcal{D}}$ or zero wt & weak OBC $\omega\|_{\partial\mathcal{D}}=0\ \&\ \frac{\partial HU\cdot\hat{n}}{\partial n}\big\|_{\partial\mathcal{D}}=\frac{\partial^2\Psi_{(-1)}}{\partial n\partial t}\big\|_{\partial\mathcal{D}}=0$
Construct exterior BCs (optimize J_b, Eq. 10) using either original $\vec{U}_{(0)}$ or recomputed $\vec{U}_{(0)}$ above (for nesting, interpolate Ψ_{b^e} from larger domain)	recompute : $H\vec{U}_{(0)}=\hat{k}\times\nabla\Psi_{(-1)}$ $-\frac{\partial}{\partial s}\left(\omega\frac{\partial\Psi_{b^e}}{\partial s}\right)=\frac{\partial}{\partial s}\left(\omega H\vec{U}_{(0)}\cdot\hat{n}\right)$ along open boundaries $-\left(\omega\frac{\partial\Psi_{b^e}}{\partial s}\right)\Big\|_{C_m^{e-}}^{C_m^{e+}}=\left(\omega H\vec{U}_{(0)}\cdot\hat{n}\right)\big\|_{C_m^{e-}}^{C_m^{e+}}$ at unknown coasts $\{C_m^e\}$ $\Psi_{b^e}\big\|_{C_m^{e-}}^{C_m^{e+}}=0$ at unknown coasts $\{C_m^e\}$ $\Psi_{b^e}\big\|_{C_k^e}=\Psi_{C_k^e}$ at known coasts $\{C_k^e\}$
Construct "certain coast" solution (Eq. 12) using Ψ_{b^e} from above	$\nabla\cdot(\omega\nabla\Psi_{(0)})=\left[\nabla\times\left(\omega H\vec{U}_{(0)}\right)\right]\cdot\hat{k}$ $\Psi_{(0)}\|_{\partial\mathcal{D}^e}=\Psi_{b^e}\equiv\begin{cases}\Psi_{b^e} & \text{if } s\in\partial\mathcal{D}^e\\ \Psi_{C_k^{ic}} & \text{if } s\in C_k^{ic}\end{cases}$
Construct interior island BCs (optimize J_{b^u}, Eq. 15) using $\Psi_{(0)}$ from above	$\left[\sum_{m\neq n}^{N^{iu}}\varpi_{nm}^{uu}+\sum_{k=1}^{M^c}\varpi_{nk}^{uc}+\varpi_{nb}^{uo}\right]\Psi_{C_n^{iu}}-\sum_{m\neq n}^{N^{iu}}\varpi_{nm}^{uu}\Psi_{C_m^{iu}}=\sum_{m\neq n}^{N^{iu}}\varpi_{nm}^{uu}\Delta_{nm}^{uu}\Psi_{(0)}+\sum_{k=1}^{M^c}\varpi_{nk}^{uc}\Psi_{(0)}(s_{nk}^{uc})+\varpi_{nb}^{uo}\Psi_{(0)}(s_{nb}^{uo})$
Solve full problem (optimize J, Eqs. (5) and (16)) using Ψ_{b^e} and $\Psi_{C_n^{iu}}$ from above	$\nabla\cdot(\omega\nabla\Psi)=\left[\nabla\times\left(\omega H\vec{U}_{(0)}\right)\right]\cdot\hat{k}$ $\Psi\|_{\partial\mathcal{D}}=\Psi_b\equiv\begin{cases}\Psi_{b^e} & \text{if } s\in\partial\mathcal{D}^e\\ \Psi_{C_k^{ic}} & \text{if } s\in C_k^{ic}\\ \Psi_{C_n^{iu}} & \text{if } s\in C_n^{iu}\end{cases}$

where $H\vec{\tilde{U}}_{(1)}$ is any test transport, $\omega(x,y)$ a positive definite weighting function and da an area element over domain $\mathcal{D}$.

The first non-divergence constraint is imposed by replacing $H\vec{\tilde{U}}_{(1)}$ in Eq. (2) using a test transport streamfunction, $\tilde{\Psi}$, formulation defined as

$$H\vec{\tilde{U}}_{(1)} = \hat{k} \times \nabla\tilde{\Psi} \tag{3}$$

where $\hat{k}$ the unit vector in the vertical. For 3D velocities, one has the choice of either working with layer-by-layer transports or directly with level-by-level velocities. If one chooses layer transports, then the only change to Eq. (3) (and in subsequent Eqs. and weighting functions) is that $H(x,y)$ is the (variable) layer thickness, not the total water depth. If one optimizes level-by-level velocities, then level-by-level test velocity streamfunctions are defined,

$$\vec{\tilde{u}}_{(1)} = \hat{k} \times \nabla\tilde{\psi}. \tag{4}$$

This imposes a horizontal non-divergence on $\vec{\tilde{u}}_{(1)}$. For cases in which $\nabla \cdot \vec{u}_{(0)}$ is important, a corrector to recover this divergence is obtained in Appendix B.

In Appendix D.1, we obtain, via the calculus of variations, the following PDE for the Ψ that minimizes J for a given set of imposed BCs, Ψ_b (to be derived):

$$\nabla \cdot (\omega\nabla\Psi) = \left[\nabla \times \left(\omega H\vec{U}_{(0)}\right)\right] \cdot \hat{k} \tag{5}$$
$$\Psi|_{\partial\mathcal{D}} = \Psi_b$$

Eq. (5) without the weighting function, ω, is fairly standard and usually obtained via the Helmholtz decomposition of a vector into nondivergent and irrotational components (e.g., Lynch, 1989; Denaro, 2003; Li et al., 2006). The weighting function $\omega(x,y)$ can be decomposed into the product of a weight based on the uncertainty in $H\vec{U}_{(0)}$ and a physically-based weight. Two intuitive choices for the physically-based weight are: $\omega = 1$, i.e. Eq. (2) minimizes the difference in the transports, and $\omega = \frac{1}{H^2}$, i.e. Eq. (2) minimizes the difference in the velocities. In practice, while these two choices give overall similar results, minimizing the difference in transports ($\omega = 1$) tends to allow larger velocities. This can exacerbate problems with over-estimating the barotropic velocity in isolated channels in complex archipelagos, hence $\omega = \frac{1}{H^2}$ (minimizing the velocity differences) is the preferred choice. Other choices could be explored, e.g. $\omega = \left\|H\vec{U}_{(0)}\right\|^{-2}$, minimizing relative velocity, or $\omega = \|\nabla H\|^{-2}$, reducing weights over steep bathymetry where $H\vec{U}_{(0)}$ may be less accurate. When working with velocity streamfunctions, ψ, $\omega = 1$ provides the velocity best fit and $\omega = \left\|\vec{u}_{(0)}\right\|^{-2}$ provides the relative velocity best fit. When implementing Eq. (5) for ψ, we often impose it at all vertical levels to ensure vertical interpolations maintain no-normal flow.

Boundary Conditions Before Eq. (5) can be solved for Ψ, the Dirichlet boundary values Ψ_b need to be optimized. Here, we derive a system of equations to obtain the best-fit Dirichlet conditions along the open boundaries and complex "external coasts", coastlines which intersect the boundary of the computational domain. The external coasts and open boundaries form the exterior boundary, $\partial\mathcal{D}^e \subset \partial\mathcal{D}$, of the complex domain. This scheme assumes that the boundary values of $\vec{U}_{(0)}$ are known with equal confidence to the interior values, which is appropriate when downscaling or when the coverage (data or feature model) extends to the boundaries. For other cases, we derive a scheme to first extend the interior velocity information to the boundaries, and then use them in the present scheme. Boundary values for "islands" (landforms in the interior of $\mathcal{D}$) are discussed in Section 3.2.

Since $H\vec{U}_{(0)}$ does not respect the divergence or coastal constraints even at the boundary (e.g. no net transport), we need best-fit boundary values which do. The cost function, J_{b^e}, defined on $\partial\mathcal{D}^e$ which optimizes candidate Dirichlet BCs, $\tilde{\Psi}_{b^e}$, to best-fit the normal transport provided by $H\vec{U}_{(0)}$ is:

$$J_{b^e}(H\vec{\tilde{U}}_{b^e}) = \frac{1}{2}\oint_{\partial\mathcal{D}^e} \omega\left[\left(H\vec{U}_{(0)} - H\vec{\tilde{U}}_{b^e}\right)\cdot\hat{n}\right]^2 ds$$

$$\Longleftrightarrow J_{b^e}(\tilde{\Psi}_{b^e}) = \frac{1}{2}\oint_{\partial\mathcal{D}^e} \omega\left(\frac{\partial\tilde{\Psi}_{b^e}}{\partial s} + H\vec{U}_{(0)}\cdot\hat{n}\right)^2 ds \tag{6}$$

where ω is the same weighting function as used in Eqs. (2)–(5), $H\vec{\tilde{U}}_{b^e}$ are the candidate boundary transports corresponding to $\tilde{\Psi}_{b^e}$, and s is the tangential coordinate to the boundary in the counter-clockwise direction.

Employing calculus of variations (Appendix D.2), we obtain a PDE along the open segments for the Ψ_{b^e} that minimizes J_{b^e}

$$-\frac{\partial}{\partial s}\left(\omega\frac{\partial\Psi_{b^e}}{\partial s}\right) = \frac{\partial}{\partial s}\left(\omega H\vec{U}_{(0)}\cdot\hat{n}\right) \tag{7}$$

along with the jump conditions at the coastal endpoints

$$-\left[\omega\left(\frac{\partial\Psi_{b^e}}{\partial s} + H\vec{U}_{(0)}\cdot\hat{n}\right)\right]\Bigg|_{C_m^{e-}}^{C_m^{e+}} = 0 \tag{8}$$

where C_m^{e+} is the end of coast m (traversing the coast counter-clockwise) and C_m^{e-} is the beginning, see Fig. 1. To ensure no-normal flow (i.e. Ψ_{b^e} constant along C_m^e), we append the following condition

$$\Psi_{b^e}\Big|_{C_m^{e-}}^{C_m^{e+}} = 0. \tag{9}$$

Physically, Eq. (8) equalizes the mismatch (weighted by ω) between $H\vec{U}_{(0)}\cdot\hat{n}$ and $H\vec{U}_{(1)}\cdot\hat{n} = -\frac{\partial\Psi_{b^e}}{\partial s}$ at both ends of a coast (i.e. between open boundary segments), while Eq. (7) equilibrates the variations in the mismatch along the open boundary segments. Enforcing both (7) and (8) thus penalizes the mismatch along all boundaries. Note that if one integrates (7) along coast m instead of an open segment (where (7) applies), one recovers (8).

Known transport information (most often in the form of a net transport between coasts) can also be included, taking advantage of the additive indeterminacy in Ψ. To do this, we identify the set of coasts, $\{C_k^e\}$, along which the values for the transport streamfunction, $\{\Psi_{C_k^e}\}$ are known and directly impose these values. As an example, consider the domain of Fig. 1 and assume that the literature reports a net 1 Sv southeast transport between C_1^e and C_2^e. We can arbitrarily pick two values for these coasts whose difference is equal to the net transport (e.g. $\Psi_{C_1^e} = 0$ and $\Psi_{C_2^e} = 1$ Sv) and include those two identity equations to impose this net transport. The final, general, system for finding the Dirichlet boundary values (separating the unknowns on the left-hand side from the knowns on the right) is

$$\begin{aligned}
&-\frac{\partial}{\partial s}\left(\omega\frac{\partial\Psi_{b^e}}{\partial s}\right) = \frac{\partial}{\partial s}\left(\omega H\vec{U}_{(0)}\cdot\hat{n}\right) \quad \text{along open boundaries}\\
&-\left(\omega\frac{\partial\Psi_{b^e}}{\partial s}\right)\Bigg|_{C_m^{e-}}^{C_m^{e+}} = \left(\omega H\vec{U}_{(0)}\cdot\hat{n}\right)\Big|_{C_m^{e-}}^{C_m^{e+}} \quad \text{at unknown coasts } \{C_m^e\}\\
&\Psi_{b^e}\Big|_{C_m^{e-}}^{C_m^{e+}} = 0 \quad \text{at unknown coasts } \{C_m^e\}\\
&\Psi_{b^e}|_{C_k^e} = \Psi_{C_k^e} \quad \text{at known coasts } \{C_k^e\}
\end{aligned} \tag{10}$$

After Eq. (10) are solved, the values for Ψ_{b^e} found at the ends of the unknown coasts, C_m^e, are applied all along their respective

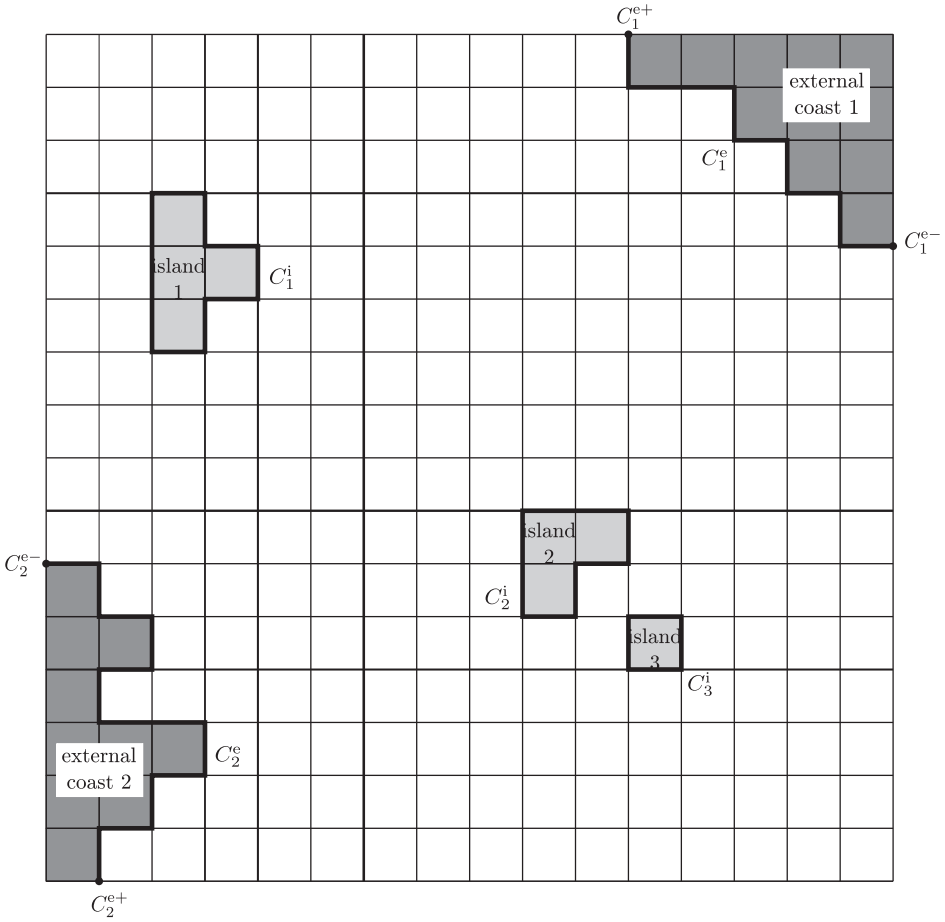

Fig. 1. Canonical computational domain, highlighting the different types of landforms and coasts.

coasts, C_m^e. For velocity streamfunctions, replace (Ψ, Ψ_{b^e}) with (ψ, ψ_{b^e}) and $H\vec{U}_{(0)}$ with $\vec{u}_{(0)}$ in Eqs. (5) and (10). The algorithm and its equations are summarized in Table 2.

Propagating interior information to the boundaries. Here we give the solution in which $\vec{U}_{(0)}$ in the interior of the complex domain, or in part of it, is known with a higher degree of confidence than $\vec{U}_{(0)}$ along the open boundary. Hence we propagate the interior information to the boundary prior to solving Eq. (10). The basic idea is to use a modified version of the best-fit Eq. (5) to perform the propagation. There are two modifications. The first modifies $\mathcal{D}$ by removing all but a single coast, C^{1cst}, (i.e. we transform the remaining land points into shallow ocean points and take advantage of the fact that $\vec{U}_{(0)} = 0$ under all land and coasts). Along this single coast we are free to impose any constant, $\Psi_{C^{1cst}}$. The second modification is to replace the Dirichlet OBCs by either the Neumann OBCs derived in Appendix D.1 or by a combination of weaker free-OBCs with ω identically zero at the boundary (to maintain a best-fit solution, Appendix D.1). Finally, the function $\omega(x, y)$ needs to be small (e.g. based on uncertainty) near the open boundaries. This gives:

$$\nabla \cdot (\omega \nabla \Psi_{(-1)}) = \left[\nabla \times \left(\omega H \vec{U}_{(0)}\right)\right] \cdot \hat{k} \tag{11}$$

$$\Psi_{(-1)}\big|_{C^{1cst}} = \Psi_{C^{1cst}}$$

and either

$$\nabla \Psi_{(-1)} \cdot \hat{n}\big|_{\partial\mathcal{D}} = -\hat{k} \times H\vec{U}_{(0)} \cdot \hat{n}\Big|_{\partial\mathcal{D}}$$

or

$$\omega|_{\partial\mathcal{D}} = 0 \quad \& \quad \text{e.g.} \quad \left.\frac{\partial HU \cdot \hat{n}}{\partial n}\right|_{\partial\mathcal{D}} = \left.\frac{\partial^2 \Psi_{(-1)}}{\partial n \partial t}\right|_{\partial\mathcal{D}} = 0$$

We then recompute $\vec{U}_{(0)}$ from the $\Psi_{(-1)}$ and use this new $\vec{U}_{(0)}$ in Eq. (10). For velocity streamfunctions, replace $\Psi_{(-1)}$ by $\psi_{(-1)}$ and $H\vec{U}_{(0)}$ by $\vec{u}_{(0)}$.

Nesting considerations. When preparing initializations for nested domains with complex multiply-connected geometries, a key consideration is consistency between the fields in coarser and finer grids. To ensure this consistency, we by-pass Eq. (10) for the fine grid, and instead interpolate the coarse-domain Ψ to obtain the fine domain Ψ_{b^e}. This is illustrated in Section 4.3.3 where we explore options for the fine-domain islands.

3.2. Core algorithm to optimize sub-tidal transports between islands and velocities near islands

To obtain the Dirichlet values along islands (Ψ_{C^i}), either transport estimates from additional sources (e.g. estimates in the literature) are used or a scheme is required to construct the necessary constant values from $\vec{U}_{(0)}$. Care is needed to ensure that the selected constant values do not produce unrealistic velocities, especially in multiply-connected archipelagos. Here we derive a system of algebraic equations (Eq. 15) for the optimized constant values of the streamfunction along islands that were uncertain, $\Psi_{C^{iu}}$ or $\psi_{C^{iu}}$, a common situation in complex domains.

"Certain coast" Solution. In order to obtain a first estimate for the unknown transports between islands and other coasts, we best-fit transports and velocities in the absence of islands (i.e. we transform

the islands into ocean points). We begin by separating $\partial\mathcal{D}$ into certain, $\partial\mathcal{D}^c$, and uncertain, $\partial\mathcal{D}^{iu}$, segments. $\partial\mathcal{D}^c$ will be comprised of $\partial\mathcal{D}^e$, the solved external boundaries (Eq. (10)), and of $\partial\mathcal{D}^{ic}$, islands $C_k^{\rm ic}$ along which we have streamfunction values, $\Psi_{C_k^{\rm ic}}$, we wish to impose (e.g. a literature estimate for the transport between $C_k^{\rm ic}$ and $C_m^{\rm e}$ added to the previously obtained Ψ_{b^e} along $C_m^{\rm e}$). We solve for the "certain coast solution", $\Psi_{(0)}$, over $\mathcal{D}$ using the PDE

$$\nabla\cdot\left(\omega\nabla\Psi_{(0)}\right)=\left[\nabla\times\left(\omega H\vec{U}_{(0)}\right)\right]\cdot\hat{k} \tag{12}$$
$$\Psi_{(0)}\big|_{\partial\mathcal{D}^c}=\Psi_{b^c}\equiv\begin{cases}\Psi_{b^e} & \text{if } s\in\partial\mathcal{D}^e\\ \Psi_{C_k^{\rm ic}} & \text{if } s\in C_k^{\rm ic}\end{cases}$$

(Table 2). Note that $\Psi_{(0)}$ is not constrained to satisfy no-normal flow along the uncertain islands. $\Psi_{(0)}$ contains useful information from the data and dynamics that went into $\vec{U}_{(0)}$ (e.g. the position of major currents relative to the coastlines, the effects of bathymetry) which will be used to determine the appropriate constant $\Psi_{C^{\rm iu}}$ along the uncertain coasts. These $\Psi_{C^{\rm iu}}$ will be used along with $(\Psi_{b^e},\Psi_{C_k^{\rm ic}})$ to complete the set of all BCs Ψ_b. Eq. (5) can then be solved to construct the final Ψ. We next define two methods for determining $\Psi_{C^{\rm iu}}$: averaging and weighted Least Squares optimization.

Averaging. The first simpler method we define is to average $\Psi_{(0)}$ along each $C_k^{\rm iu}$ and use those averages for Ψ_b in Eq. (5) as

$$\Psi_b=\begin{cases}\Psi_{b^e} & \text{if } s\in\partial\mathcal{D}^e\\ \Psi_{C_k^{\rm ic}} & \text{if } s\in C_k^{\rm ic}\\ \dfrac{\oint_{C_k^{\rm iu}}\Psi_{(0)}ds}{\oint_{C_k^{\rm iu}}ds} & \text{if } s\in C_k^{\rm iu}\end{cases} \tag{13}$$

In practice, we found that this averaging only works if the differences between the finally determined Ψ and $\Psi_{(0)}$ are localized around each island (i.e. only small perturbations introduced at other islands). In general, one can not require such localization assumptions. Hence, we derive a new, robust method for constructing $\Psi_{C^{\rm iu}}$. We compare results using these two methods in Section 4.

Weighted Least Squares optimization. The optimization best fits the inter-island transports to the minimum inter-island transports as calculated from $\Psi_{(0)}$ in order to find $\Psi_{C^{\rm iu}}$ that produce a balanced and smooth velocity field, e.g. with no unrealistically large velocities. In the uncertain straits, the goal is to minimize the difference between the minimum net transports between islands estimated from $\Psi_{(0)}$ and the net transports between islands with $\Psi_{C^{\rm iu}}$ constant along each island. Alternatively one can minimize the differences between the average barotropic velocities between islands from $\Psi_{(0)}$ and using $\Psi_{C^{\rm iu}}$. In Section 3.2.1 we show how to compute weights to select between fitting the transports or the barotropic velocities. The addition of weak constraints to provide additional bounds on the velocity is presented in Section 3.2.2.

We define M^c as the number of coasts in $\partial\mathcal{D}^c$ and N^{iu} as the number of coasts in $\partial\mathcal{D}^{iu}$. The global optimization functional to find the $\Psi_{C^{\rm iu}}$ is

$$\begin{aligned}J_{b^u}\left(\Psi_{C_1^{\rm iu}},\ldots,\Psi_{C_{N^{iu}}^{\rm iu}}\right)=&\frac{1}{2}\sum_{n=1}^{N^{iu}}\sum_{m=n+1}^{N^{iu}}\left[\varpi_{nm}^{\rm uu}\left(\Psi_{C_n^{\rm iu}}-\Psi_{C_m^{\rm iu}}-\Delta_{nm}^{uu}\Psi_{(0)}\right)^2\right]\\&+\frac{1}{2}\sum_{n=1}^{N^{iu}}\sum_{k=1}^{M^c}\left[\varpi_{nk}^{\rm uc}\left(\Psi_{C_n^{\rm iu}}-\Psi_{(0)}(s_{nk}^{uc})\right)^2\right]\\&+\frac{1}{2}\sum_{n=1}^{N^{iu}}\left[\varpi_{nb}^{\rm uo}\left(\Psi_{C_n^{\rm iu}}-\Psi_{(0)}(s_{nb}^{uo})\right)^2\right]\end{aligned} \tag{14}$$

Eq. (14) is comprised of three terms: (i) a double summation to optimize the transport between all pairs of uncertain coasts, $C^{\rm iu}$; (ii) a double summation to optimize the transport between all pairs of uncertain and certain coasts, $C^{\rm c}$; and (iii) a single summation to optimize the transport between each of the uncertain coasts and the open boundaries of the complex domain. These three terms are derived in Appendix D.3. Note that the physical constraints on this optimization come from $\Psi_{(0)}$ (e.g. if $\Psi_{(0)}$ contains a strong current between two islands, the minimization target value of the first term, $\Delta_{nm}^{uu}\Psi_{(0)}$, contains the minimum transport of that current). We utilize the superscript notation:*uu* for weights and differences between pairs of uncertain coasts; *uc* between uncertain and certain coasts; and *uo* between uncertain coasts and the open boundaries. The first double summation in Eq. (14) measures the weighted ($\varpi_{nm}^{\rm uu}$) difference between the optimized net transport, $\Psi_{C_n^{\rm iu}}-\Psi_{C_m^{\rm iu}}$, between the pairs of coasts and the minimum net transport, $\Delta_{nm}^{uu}\Psi_{(0)}$, computed from the certain coast solution, $\Psi_{(0)}$. The second double summation measures the weighted ($\varpi_{nk}^{\rm uc}$) difference between the optimized $\Psi_{C_n^{\rm iu}}$ and $\Psi_{(0)}(s_{nk}^{uc})$, the value of $\Psi_{(0)}$ along $C_n^{\rm iu}$ which minimizes the net transport (estimated by $\Psi_{(0)}$) between $C_n^{\rm iu}$ and $C_k^{\rm c}$. s_{nk}^{uc} is the point along $C_n^{\rm iu}$ at which $\Psi_{(0)}$ attains this value. The final single summation measures the weighted ($\varpi_{nb}^{\rm uo}$) difference between the optimized $\Psi_{C_n^{\rm iu}}$ and $\Psi_{(0)}(s_{nb}^{uo})$, the value of $\Psi_{(0)}$ along $C_n^{\rm iu}$ which minimizes the net transport (estimated by $\Psi_{(0)}$) between $C_n^{\rm iu}$ and $\partial\mathcal{D}^o$. s_{nb}^{uo} is the point along $C_n^{\rm iu}$ at which $\Psi_{(0)}$ attains this value. The first double sum provides the algorithm robustness to non-localized changes from imposing the $\Psi_{C^{\rm iu}}$, while the second two provide a pathway for the absolute value of Ψ_{b^e} (Appendix D.3).

The least square minimum of J_{b^u} in (14) is computed by setting gradients with respect to $\Psi_{C_n^{\rm iu}}$'s equal to zero. The result is given by:

$$\begin{aligned}&\left[\sum_{\substack{m=1\\m\neq n}}^{N^{iu}}\varpi_{nm}^{\rm uu}+\sum_{k=1}^{M^c}\varpi_{nk}^{\rm uc}+\varpi_{nb}^{\rm uo}\right]\Psi_{C_n^{\rm iu}}-\sum_{\substack{m=1\\m\neq n}}^{N^{iu}}\varpi_{nm}^{\rm uu}\Psi_{C_m^{\rm iu}}\\&\quad=\sum_{\substack{m=1\\m\neq n}}^{N^{iu}}\varpi_{nm}^{\rm uu}\Delta_{nm}^{uu}\Psi_{(0)}+\sum_{k=1}^{M^c}\varpi_{nk}^{\rm uc}\Psi_{(0)}(s_{nk}^{uc})+\varpi_{nb}^{\rm uo}\Psi_{(0)}(s_{nb}^{uo})\end{aligned} \tag{15}$$

Eq. (15) represents a system of N^{iu} equations that we solve to obtain the constant values of transport streamfunction ($\Psi_{C_n^{\rm iu}}$) along the coastlines in $\partial\mathcal{D}^{iu}$. These streamfunction values, which smooth the velocity field, are then included as Dirichlet BCs to then solve (5).

$$\Psi_b=\begin{cases}\Psi_{b^e} & \text{if } s\in\partial\mathcal{D}^e\\ \Psi_{C_k^{\rm ic}} & \text{if } s\in C_k^{\rm ic}\\ \Psi_{C_n^{\rm iu}} & \text{if } s\in C_n^{\rm iu}\end{cases} \tag{16}$$

Imposing additional inter-island transport constraints. If there exists any additional transport information that can be imposed, for example a known transport $\Delta_{nm}^{\rm imp}\Psi$ between a specific pair of islands both in $\partial\mathcal{D}^{iu}$, the corresponding $\Delta_{nm}^{uu}\Psi_{(0)}$ (Appendix D.3) would be replaced:

$$\Delta_{nm}^{uu}\Psi_{(0)}=\begin{cases}\Delta_{nm}^{\rm imp}\Psi & \text{if imposing transport}\\ \Psi_{(0)}(s_{nm}^{uu})-\Psi_{(0)}(s_{mn}^{uu}) & \text{otherwise}\end{cases} \tag{17}$$

and the corresponding $\varpi_{nm}^{\rm uu}$ would be increased to ensure this imposed constraint is weighted much more heavily than any of

the constraints derived from $\Psi_{(0)}$. This is illustrated in Section 4.3.2. If the transport being imposed is less certain, then one would not increase the weight as much (i.e. multiply the weight needed to enforce $\Delta^{\text{imp}}_{nm}\Psi$ by an uncertainty-based weight).

3.2.1. Constructing weights using the Fast Marching Method (FMM)

We now discuss the selection of the weighting functions to be used in Eq. (15). As for ω (discussion following Eq. (5)), we can decompose these weights into the product of uncertainty-based and physically-based weights.

The primary purpose of the physically-based weights is to ensure that the optimization functional weights the transport differences between adjacent coasts more heavily that those between widely separated coasts. One class of such weights can be constructed by using the minimum distance between a pair of coasts, d_{nm}, such as $\varpi^{\text{uu}}_{nm} = (d_{global\ min}/d_{nm})^2$ where the weight is nondimensionalized by minimum distance between all pairs of coasts, $d_{global\ min}$. A second class can be obtained by integrating Eq. (3) along a path, S_{nm}, between two coasts, C_n and C_m, to get

$$\int_{S_{nm}} H\vec{U}\cdot\hat{n}\,d\mathcal{S} = \int_{S_{nm}} \hat{k}\times\nabla\Psi\cdot\hat{n}\,d\mathcal{S}$$

$$\langle\vec{U}\rangle_{nm}A_{nm} = \int_{S_{nm}} \frac{\partial\Psi}{\partial\mathcal{S}}\,d\mathcal{S}$$

$$= \Psi_{C_n} - \Psi_{C_m} \tag{18}$$

where $\langle\vec{U}\rangle_{nm}$ is the average barotropic velocity along path S_{nm} and A_{nm} is the cross-sectional area of the ocean along that path. The path between the two coasts that corresponds to the minimum cross-sectional area, $\mathcal{A}_{nm}$, will have the maximum $\langle\vec{U}\rangle_{nm}$ Therefore, comparing Eqs. (14) and (18), a weighting function which will lead to minimizing the average barotropic velocity is $\varpi^{\text{uu}}_{nm} = (\mathcal{A}_{global\ min}/\mathcal{A}_{nm})^2$, where again ϖ^{uu}_{nm} is nondimensionalized by the minimum $\mathcal{A}_{nm}$ between all coasts and between all coasts and open boundaries, $\mathcal{A}_{global\ min}$. Note: if d_{nm} is the distance along the shortest path in the ocean, then similar arguments can be used to show $\varpi^{\text{uu}}_{nm} = (d_{global\ min}/d_{nm})^2$ is equivalent to minimizing the transport. The effects of different choices for the weights (ϖ^{uu}_{nm}, ϖ^{uc}_{nk} and ϖ^{uo}_{nb}) are illustrated in Section 4.3.1. For the case of velocity streamfunctions, ψ, Eq. (18) reduces to $\langle\vec{u}\rangle_{nm}d_{nm} = \psi_{C_n} - \psi_{C_m}$. Hence for ψ, minimizing the maximum $\langle\vec{u}\rangle_{nm}$ requires $\varpi^{\text{uu}}_{nm} = (d_{global\ min}/d_{nm})^2$.

To efficiently find the minimum $\mathcal{A}_{nm}$ among all paths between a pair of islands, we employ the FMM (see Agarwal 2009; Haley et al., 2014), which solves an Eikonal equation for a monotonically expanding front:

$$|\nabla\mathcal{T}(x,y)|\mathcal{F}(x,y) = 1 \tag{19}$$

where $\mathcal{F}(x,y)$ is the scalar speed and $\mathcal{T}(x,y)$ is the minimum time to reach any point in the domain from a given starting point (x_0,y_0). To obtain the minimum area, $\mathcal{A}_{nm}$, or the minimum distance, d_{nm} we set

$$\mathcal{F}(x,y) = \begin{cases} \frac{1}{H(x,y)} & \text{to find } \mathcal{A}_{nm} \\ 1 & \text{to find } d_{nm} \end{cases}$$

and $\mathcal{T}|_{C^{\text{i}}_n} = 0$ along one island (C^{i}_n). We then solve Eq. (19) for $\mathcal{T}(x,y)$ using the FMM. With these choices for speed $\mathcal{F}$, the minimum time to reach the second island, $\min\left(\mathcal{T}|_{C^{\text{i}}_m}\right)$, is numerically equal to $\mathcal{A}_{nm}$ or d_{nm}. Since we are only interested in the value of the minimal cross-sectional area and not its path, we do not need to perform a back-tracking step to find that path (e.g., Lolla et al., 2012, 2014a,b; Lermusiaux et al., 2015).

3.2.2. Weak bounds on velocity and transport constraints

We finally present one optional variation of our algorithm to find the inter-island transports: the inclusion of additional weak constraints on the barotropic velocity. Focusing on the example of the flow between a pair of islands, assume that Eq. (15) is being solved using the minimum area for the physically-based portion of the weighting. Then, prior to solving Eq. (15), estimates exist for both the target transport, $\Delta^{uu}_{nm}\Psi_{(0)}$, and the minimum cross-sectional area, $\mathcal{A}_{nm}$, between the islands. Using Eq. (18), the corresponding average barotropic velocity, $\langle\vec{U}\rangle_{nm}$ can also be computed. If an independent upper bound, V_{lim}, exists for the mean barotropic velocity between the islands (e.g. from literature or a precautionary upper bound), then we modify the definition of $\Delta^{uu}_{nm}\Psi_{(0)}$ (Appendix D.3) to be

$$\Delta^{uu}_{nm}\Psi_{(0)} = \begin{cases} V_{lim}\,\mathcal{A}_{nm}\,\text{sign}\left(\Psi_{(0)}(s^{uu}_{nm}) - \Psi_{(0)}(s^{uu}_{mn})\right) & \text{if } |\langle\vec{U}\rangle_{nm}| > V_{lim} \\ \Psi_{(0)}(s^{uu}_{nm}) - \Psi_{(0)}(s^{uu}_{mn}) & \text{otherwise} \end{cases} \tag{20}$$

and use this in Eq. (15). Eq. (20) is similar to Eq. (17). Differences here are that (i) we apply weak upper and lower bounds to the velocity but do not force a specific transport hence we do not increase the weights and (ii) we obtain the transport based on the velocity estimates. For the transport between islands and external coasts, the same change applies, except that $\Psi_{(0)}(s^{uc}_{nk})$ is replaced by $\Psi_{C^{\text{c}}_k} + V_{lim}\,\mathcal{A}_{nm}\,\text{sign}(\Delta^{uc}_{nk}\Psi_{(0)})$ (similarly for the transport between islands and the exterior open boundary). The application of these bounds is illustrated in Section 4.3.1. This can be adapted to also provide lower bounds for the mean barotropic velocities or directly bound the transports. Uncertainty information can also be incorporated into the weights.

4. Applications

In Section 4.1 we illustrate our core algorithm to optimize subtidal velocities and transports in complex domains around the Hawaiian islands of Kauai and Niihau. We then compare our core algorithm to the result of an averaging method (Eq. 13) to obtain the streamfunction values along the uncertain islands and to the result of a spin-up IC. Subsequent simulations starting from the three ICs show that our optimized IC does a significantly better job at reproducing the historically observed circulation patterns. In Section 4.2, we consider the Taiwan region and compare the results of our optimized ICs, ICs using $\Psi_{C^{\text{iu}}}$ from averaging and two spin-up ICs. We also compare hindcast simulations initialized from four different fields to independent *in situ* data off the coast of Taiwan. The hindcasts from reduced physics ICs outperform those from spin-up ICs, with the hindcast from our optimized ICs providing again the overall best fit to data. In the Philippine Archipelago, Section 4.3, our optimization removes spurious velocities introduced by the averaging method. In light of the many islands, in Section 4.3.1 we explore the impacts of different choices of weights (Section 3.2.1) and the application of velocity limits (Section 3.2.2). In Section 4.3.2, we demonstrate imposing inter-island transports in selected straits (Eq. 17) in conjunction with the optimization. Finally in Section 4.3.3, we exemplify our optimization in nested configurations. Note that in all these examples we compare methods for constructing $\vec{u}_{(1)}$, $\vec{u}_{(2)}$ and $H\vec{U}_{(1)}$. The final initial w estimate is computed at a later step, Eq. (C.6).

4.1. Hawaiian Islands region

We illustrate the steps of our optimization method in a 269×218 km domain around the island of Kauai, which also encompasses the island of Niihau and the western tip of Oahu

(Fig. 2). This domain was employed for the Kauai-09 field exercise (July 28–August 8, 2009). We discretize the domain with 1 km horizontal resolution and 90 vertical levels in a terrain-following coordinate system. We objectively analyze a combination of CTDs from GTSPP (July 1–24, 2009) with a corrected July WOA01 climatology to create July 25, 2009 ICs on flat levels. The correction shifted the mean salinity profile in the upper 100 m to be consistent with the 2009 profiles. A 7 day analysis SST from the UK NCOF Operational SST and Sea Ice for July 25, 2009 is combined with the mapped T in a 40 m mixed layer with a 7 m exponential decay in the transition zone. $\vec{u}_{(0)}$ is then constructed by a combination of (i) velocities in geostrophic balance with the 3D T/S fields using a 2000 m level of no-motion (LNM), (ii) velocity anomalies derived from SSH anomaly estimates for July 25, 2009 obtained from the Colorado Center for Astrodynamics Research (CCAR; Leben et al., 2002), and, (iii) feature models for the North Hawaiian Ridge Current (north of Oahu) and the Hawaiian Lee Current (south of Oahu) which add broad northwesterly currents that become more westerly with increasing latitude. The surface velocity anomalies, $\Delta\vec{u}_{SSH}$, derived from the SSH anomaly, $\Delta\eta_{SSH}$, are constructed from geostrophy and hydrostatics using

$$\hat{k} \times f\Delta\vec{u}_{SSH} = -g\nabla\Delta\eta_{SSH} \tag{21}$$

where f is the Coriolis factor and g the acceleration due to gravity. The $\Delta\vec{u}_{SSH}$ are extended in the vertical using a Gaussian profile with a 250 m decay scale. After the superposition, the simple bathymetry constraints are applied, leading to $\vec{u}_{(0)}$ (Fig. 2(a)). We fit $\vec{u}_{(1)}$ to the level-by-level coastal constraints (Fig. 2(b)), interpolate to the terrain-following coordinates and construct $H\vec{U}_{(0)}$ from the

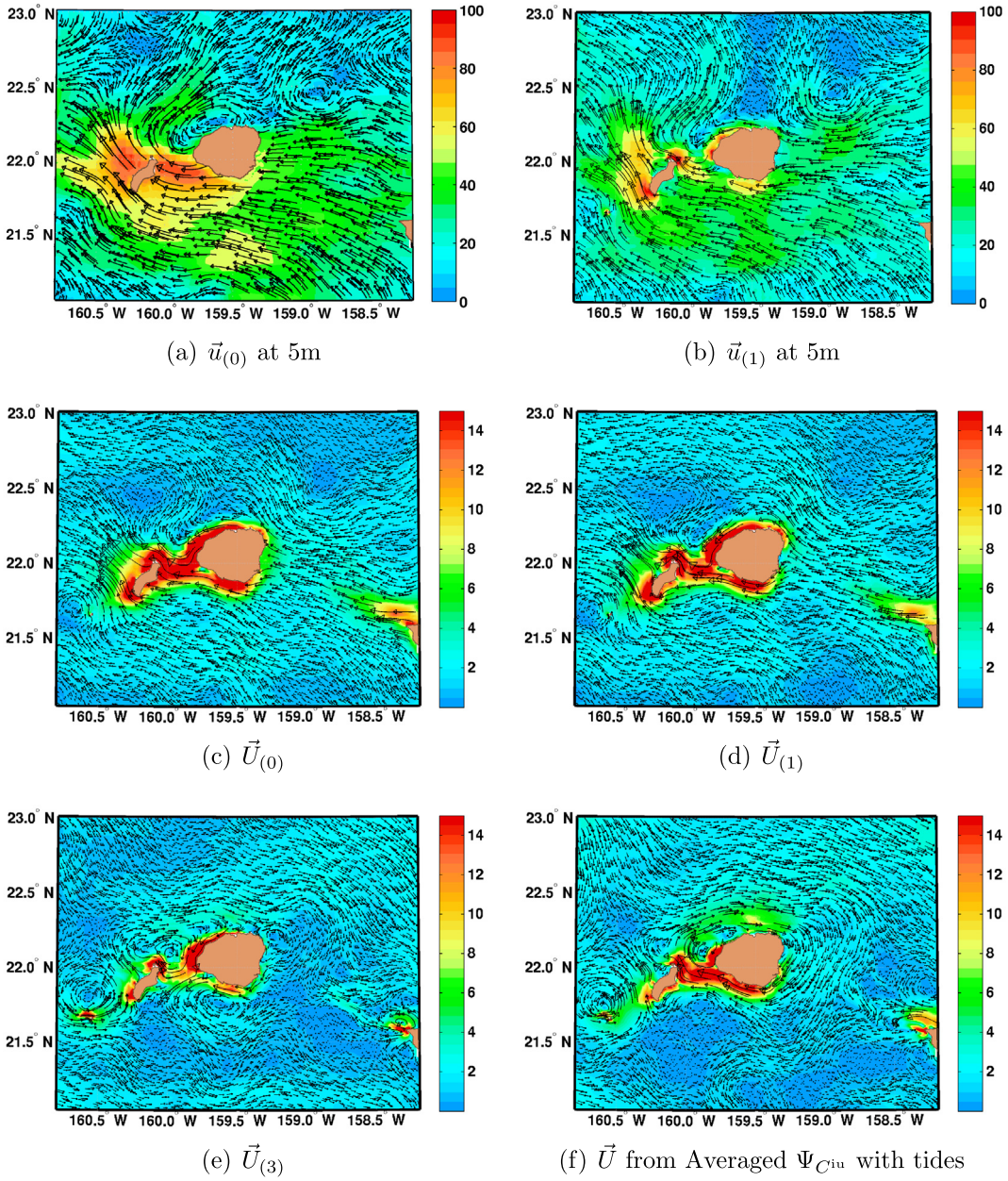

(a) $\vec{u}_{(0)}$ at 5m (b) $\vec{u}_{(1)}$ at 5m

(c) $\vec{U}_{(0)}$ (d) $\vec{U}_{(1)}$

(e) $\vec{U}_{(3)}$ (f) $\vec{U}$ from Averaged $\Psi_{C^{\text{iu}}}$ with tides

Fig. 2. Illustrating the steps in optimizing velocities and transports. (a) First guess velocity field on flat levels. (b) Applying level-by-level coastal/bathymetric constraints on flat levels. (c) Resulting first guess transport (after interpolation to terrain-follow grid). (d) Applying coastal/bathymetric constraints to transport. (e) Superimposing tides. This is the final IC estimate, result of our optimization. (f) IC obtained using averaging to impose no-normal flow, shown for comparison.

interpolated $\vec{u}_{(1)}$ (Eq. 1, Fig. 2(c)). Even though $\vec{u}_{(1)}$ has been fit to coasts, $\vec{U}_{(0)}$ has not and it still has velocities into the coasts of Kauai and Niihau. Thus, we next fit $\vec{U}_{(1)}$ to the coastal constraints, using our optimization (Eq. 15, Fig. 2(d)). We then rescale $\vec{U}_{(1)}$ for the subtidal free surface ($\vec{U}_{(2)}$, not shown) and finally superimpose barotropic tides, created using Logutov and Lermusiaux, 2008 with boundary forcing from OTIS (Egbert and Erofeeva, 2002), to obtain $\vec{U}_{(3)}$ (Fig. 2(e)). For comparison, we also present an initialization from geostrophy, without the level-by-level optimization, with the subtidal barotropic velocity obtained using $\Psi_{C^{iu}}$ from averaging via Eq. (13) and with barotropic tides superimposed (Fig. 2(f)). The averaging overestimates the transport between the islands.

Fig. 3 compares the initial evolution of three simulations: one using the full optimization IC of Fig. 2(e), the second using the averaging IC of Fig. 2(f)) and the third a spin-up from zero with tidal forcing added. These simulations were made using the MSEAS PE model (Appendix A and HL10) and forced with atmospheric fluxes from NOGAPS and the barotropic tides described above. To compare the transports between Kauai and Niihau, Fig. 3(a)–(f) show the 24 h time averages of $\vec{U}$ at the beginning of the simulation and after an initial adjustment to the PE dynamics (4 days). Both the reduced physics IC using $\Psi_{C^{iu}}$ from averaging and the spin-up IC overestimate the transports between Kauai and Niihau, even after the initial adjustment. Both also have an excessively strong transport inflow along the northern coast of Oahu (21.5 N,158 W). The flow across f/H contours is due in part to the inability of the sparse TS data, coarse TS climatology and the relatively coarse SSH to resolve topographic effects. This would also be an issue when downscaling from an insufficiently resolved model. A sufficiently resolved TS or downscaling from a sufficiently resolved model would resolve topography and remove spurious

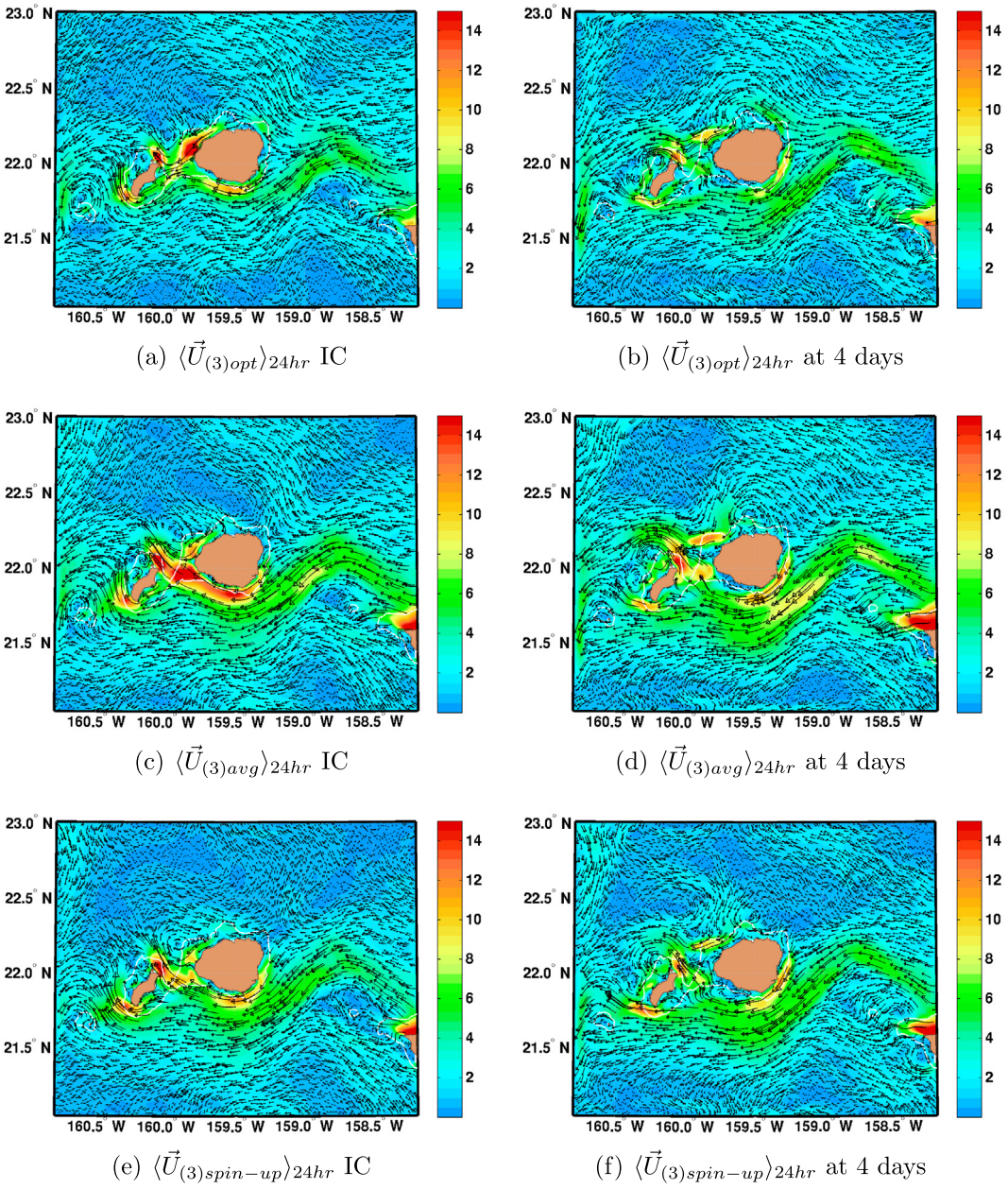

Fig. 3. Comparing 24 h-averaged velocity, $\langle\vec{U}\rangle_{24hr}$, from 3 simulations (at initial time and after 4 days). (a), (b) Simulation from optimized ICs. (c), (d) Simulation from ICs using averaged $\Psi_{C^{iu}}$. (e), (f) Simulation from spin-up ICs. Both averaged and spin-up ICs over-estimate transport between islands of Kauai and Niihau.

cross isobath flow. The optimization process drives the velocities towards the minimum transport $\Psi_{(0)}$ between these islands that is in accord with the initial guess. Since none of the initial TS, SSH, nor feature models contained strong initial guess currents between the islands, the optimized currents are diverted away from the channel and around the topography, much more closely following vorticity contours (f/H if that is the dominant term). "Averaging" merely splits the transport evenly around each island, which concentrates the flow between them. The initial spin-up also blindly splits the transport around each island. In real-time exercises, even the addition of data assimilation of the available sparse data did not correct the initial transports (not shown). Hence, the optimization (especially Eq. (15)) provides additional information on the inter-island transports which enables it to produce superior ICs to those from spin-up or "averaging".

Fig. 4(a) shows the 50 m temperature from day 4 of the simulation from optimized ICs. Differences in the 50 m temperature between the run from averaged $\Psi_{C^{iu}}$ IC and our optimized IC, and between the spin-up IC and the optimized IC, are shown in Fig. 4(c) and (d), respectively. The differences are significant, O(1–1.5 °C). Large patches of higher differences to the Northwest of Kauai by day 4 start as smaller regions off the Northern tip of Niihau and are advected to the north. These differences are directly attributable to the difference in transports. The differences in temperature between the 3 simulations continue to grow throughout the 2 week simulation (Fig. 4(b)), even though the transports become more similar to each other (not shown). This indicates that initial kinetic energy errors are transferred to potential energy errors, as hinted in the problem statement.

The circulation pattern of the optimized solution is corroborated by data. Qiu et al. (1997) produced a spaghetti diagram of surface drifter tracks around the Hawaiian islands for the period 1989–1996. Many more drifters passed south or north of Kauai/Niihau than crossed between them. Chavanne et al. (2007) produced a map of surface currents for 9 April 2003, using altimetry and high frequency radar. A strong westward current is seen south of Kauai/Niihau with only a small current between them. Firing and Brainard (2004) examined 10 years of shipboard ADCP from 1990–2000. Among their conclusions was that the North Hawaiian Ridge Current flowed (westward) to the south of Kauai/Niihau. The common element, namely the current being primarily around Kauai/Niihau rather than between them, is much more faithfully represented using the optimization ICs rather than the averaging or spin-up ICs. Even a variational initialization could benefit by starting from the optimized ICs. Finally, we stress again that during a numerical "model adjustment" of too inaccurate (too large or too small) velocities, both the density and velocity fields are modified. Even if the velocities are corrected by such adjustments, the modeled fields still have some memory of the erroneous initial velocity (the adjustment is dynamical after all). Such errors can thus damage the field estimation for some time, especially if the erroneous inter-island velocities are well within the interior of the modeling domain, in which case their dynamical effects could remain there for a significant duration. In fact, it is likely that only data assimilation could correct these effects. Of course, even if there is sufficient data to correct these effects, assimilating into fields with smaller errors reduces the potential for shock.

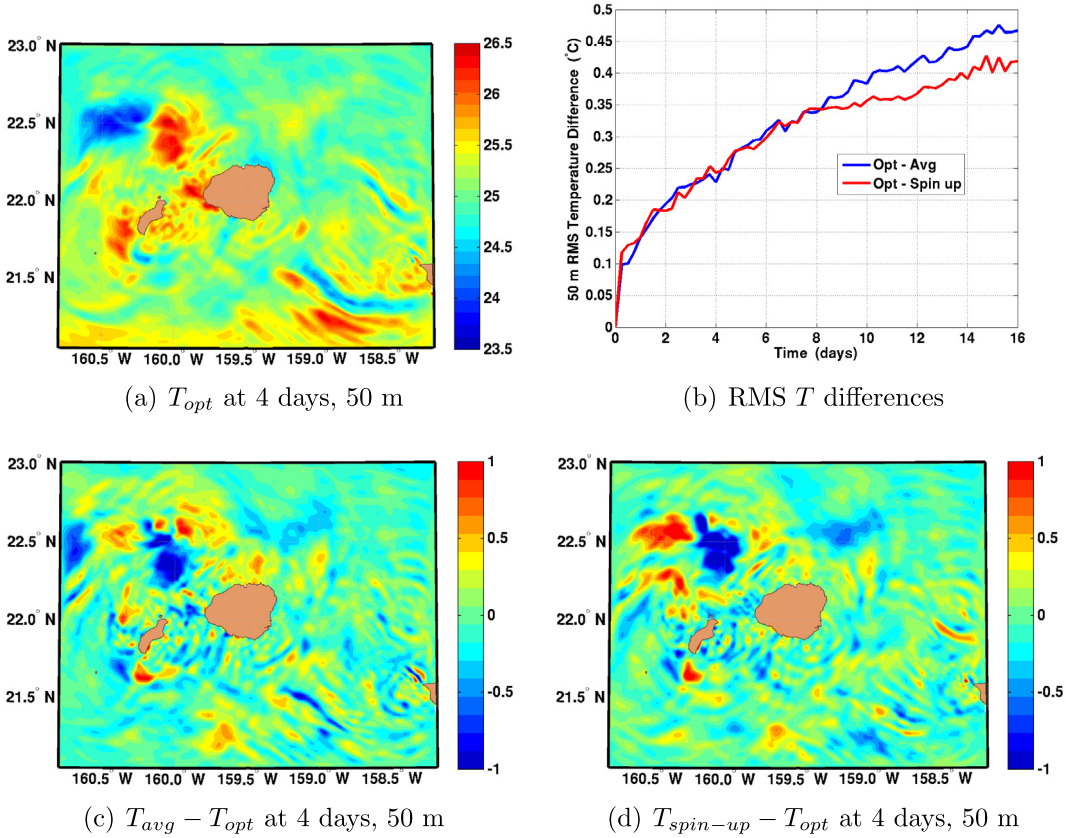

(a) T_{opt} at 4 days, 50 m

(b) RMS T differences

(c) $T_{avg} - T_{opt}$ at 4 days, 50 m

(d) $T_{spin-up} - T_{opt}$ at 4 days, 50 m

Fig. 4. Comparing temperature at 50 m from the same 3 simulations as on Fig. 3. (a) Simulation from optimized ICs. (b) Time history of RMS differences between simulations. (c) Simulation from ICs using averaged $\Psi_{C^{iu}}$. (d) Simulation from spin-up ICs. The erroneous transports of the averaged and spin-up ICs (Fig. 3) have led to growing differences in the tracer fields throughout the 2 week simulations.

4.2. Taiwan–Kuroshio region

We next consider a 1125 × 1035 km domain off the southeast coast of China encompassing Taiwan and the Kuroshio. This domain was employed for one of the Quantifying, Predicting and Exploiting uncertainty experiments during Aug 13–Sep 10, 2009 (Gawarkiewicz et al., 2011). We discretize the domain with 4.5 km horizontal resolution and 70 vertical levels in a terrain-following coordinate system (HL10). For the initialization, we objectively analyze a summer climatology T/S data set created from HydroBase 2 (Lozier et al., 1995) and World Ocean Atlas 2001 (WOA-01; Stephens et al., 2002; Boyer et al., 2002). We compute $\vec{u}_{(0)}$ using the thermal wind equations with a 1000 m LNM and imposing the simple bathymetry constraints. We then construct $\vec{u}_{(1)}$, satisfying the level-by-level coastal constraints, interpolate to terrain-following coordinates and construct the first-guess

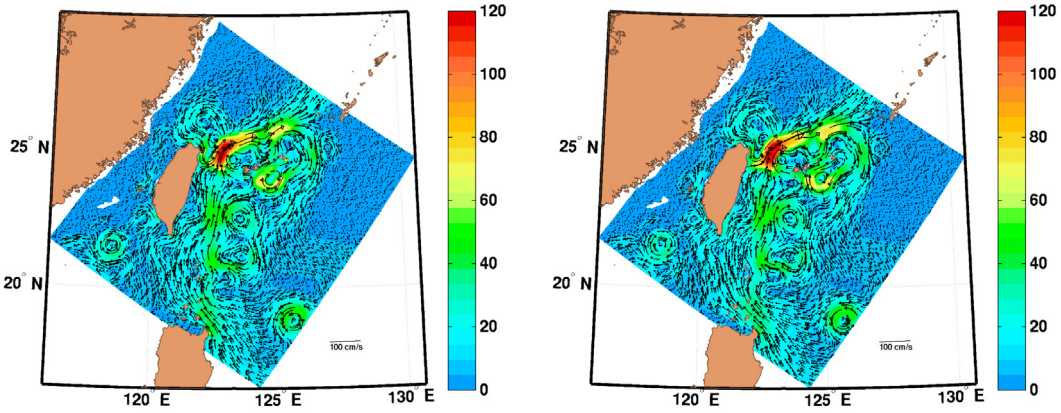

(a) 25 m $\vec{u}_{opt}$ IC (b) 25 m $\vec{u}_{avg}$ IC

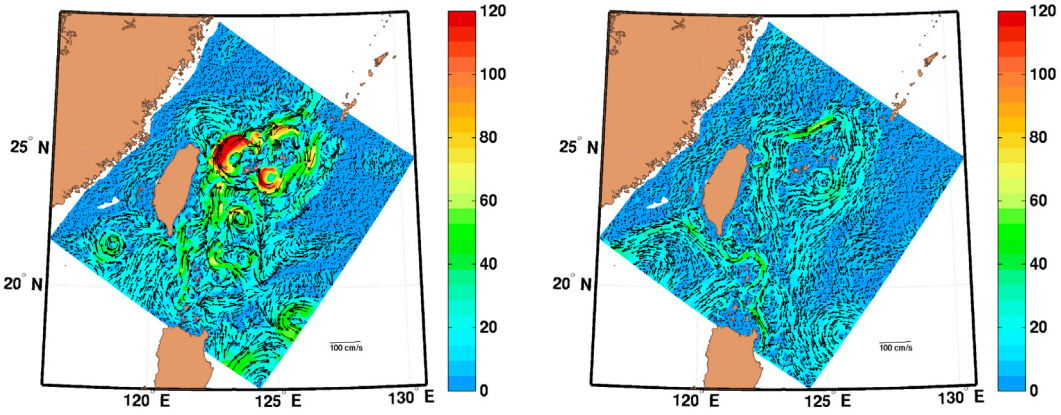

(c) 25 m $\vec{u}_{spin-up1}$ after 12.5 d (d) 25 m $\vec{u}_{spin-up2}$ after 12.5 d

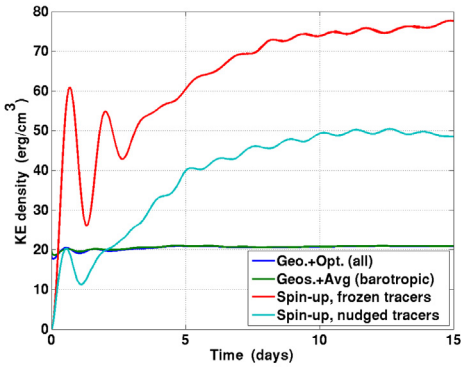

(e) KE per unit volume for runs (a)-(d)

Fig. 5. Subtidal velocity adjustment. (a) Initial velocity at 25 m, from geostrophy and optimization between islands. (b) Initial velocity at 25 m from geostrophy and averaging of island BCs for barotropic mode only. Without level-by-level optimization, initial velocities enter coasts, e.g.: southern end of Taiwan, Luzon and neighboring islands, and islands along Ilan ridge. (c) Spin-up from zero holding tracers constant. (d) Spin-up from zero but with nudging tracers at open boundaries to ICs. (e) KE per unit volume for runs initialized from (a), (b) and spin up runs (c), (d). KE relatively uniform for ICs from geostrophy. Although KE stabilized in all runs, spin-up simulations still have not developed a Kuroshio.

sub-tidal transport $H\vec{U}_{(0)}$ from the interpolated $\vec{u}_{(1)}$ (Eq. 1). We then fit $\vec{U}_{(1)}$ to the coastal constraints, using our optimization (Eq. 15).

We compare the 25 m velocity from the above initialization (Fig. 5(a)) to three other initializations. The first starts from the same $\vec{u}_{(0)}$, does not apply the level-by-level optimization and constructs a nondivergent $\vec{U}$ using $\Psi_{C^{iu}}$ obtained by averaging (Eq. (13), Fig. 5(b)). The other two ICs are spin-ups from zero velocity, the first "freezing" tracers at the initial values (Fig. 5(c)), the

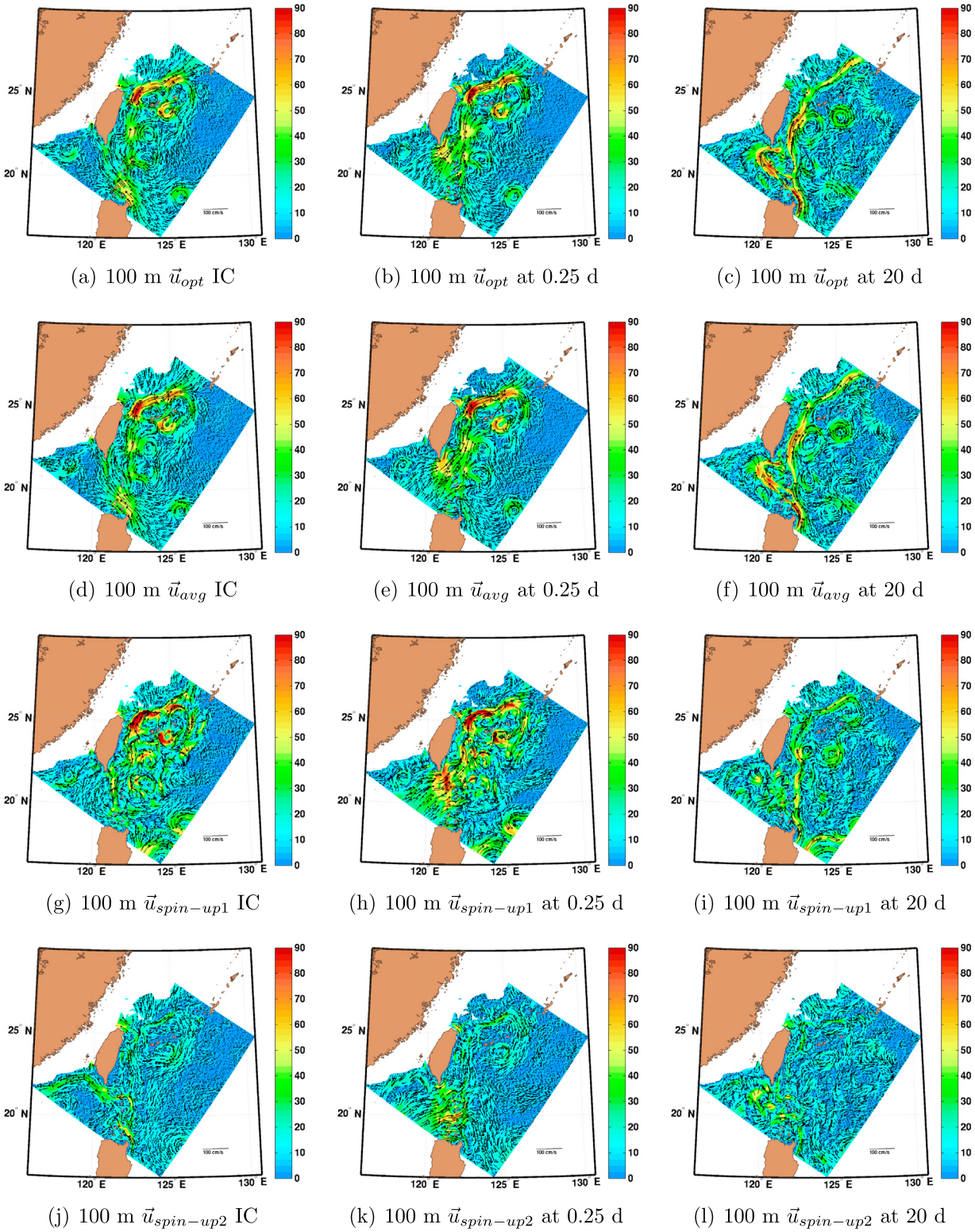

(a) 100 m $\vec{u}_{opt}$ IC (b) 100 m $\vec{u}_{opt}$ at 0.25 d (c) 100 m $\vec{u}_{opt}$ at 20 d

(d) 100 m $\vec{u}_{avg}$ IC (e) 100 m $\vec{u}_{avg}$ at 0.25 d (f) 100 m $\vec{u}_{avg}$ at 20 d

(g) 100 m $\vec{u}_{spin-up1}$ IC (h) 100 m $\vec{u}_{spin-up1}$ at 0.25 d (i) 100 m $\vec{u}_{spin-up1}$ at 20 d

(j) 100 m $\vec{u}_{spin-up2}$ IC (k) 100 m $\vec{u}_{spin-up2}$ at 0.25 d (l) 100 m $\vec{u}_{spin-up2}$ at 20 d

Fig. 6. Comparing 100 m velocity fields from simulations (horizontally: at initial time, after 0.25 day and after 20 days) initialized from four different ICs. (a)–(c) Optimized ICs. (d)–(f) Averaged $\Psi_{C^{iu}}$ ICs. (g)–(i) Spin-up (frozen tracer) ICs. (j)–(l) Spin-up (nudged tracer) ICs. Results include: the two reduced physics, optimized and averaged, ICs better maintain Kuroshio. Simulation from spin-up using nudged tracers is losing its Kuroshio.

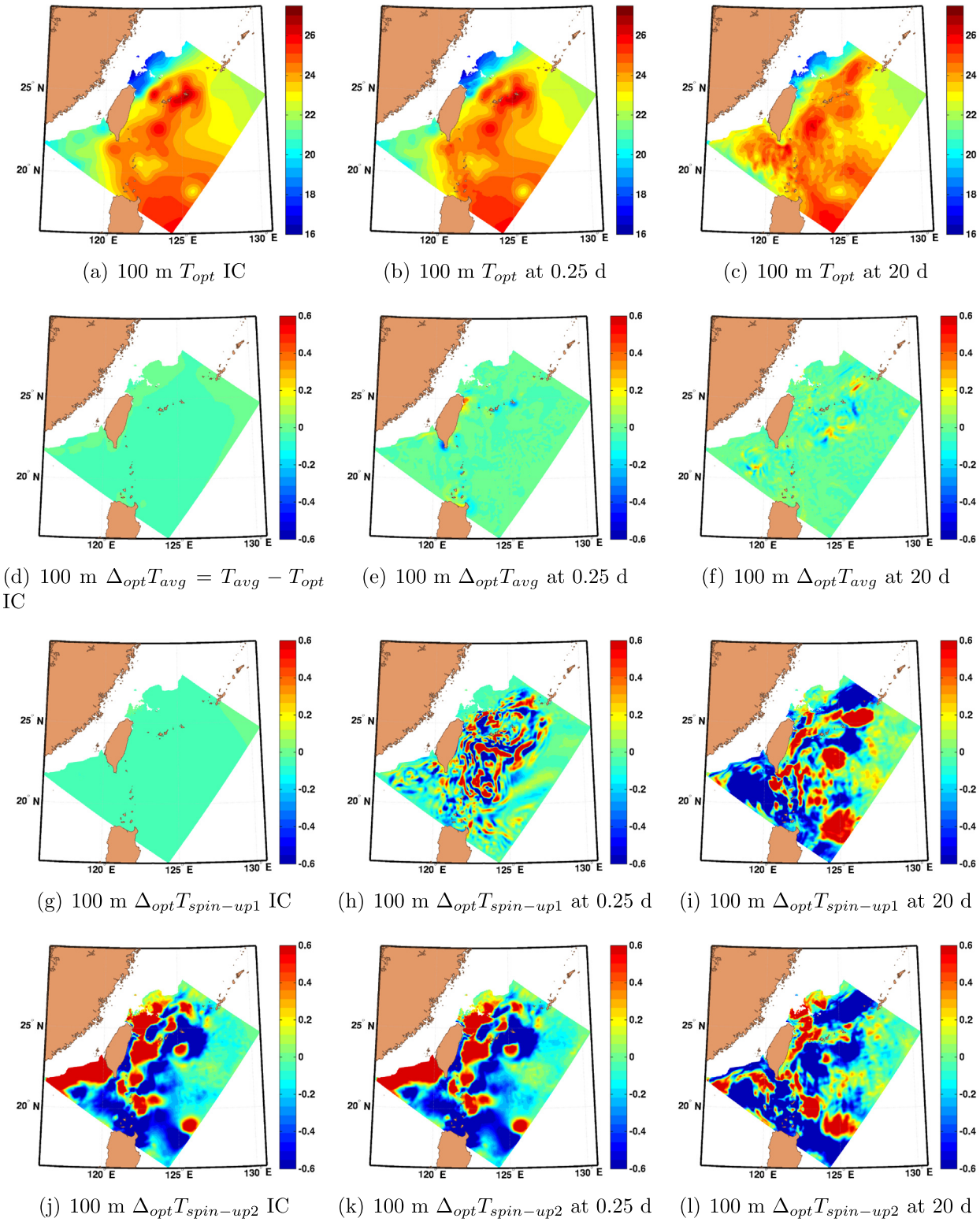

(a) 100 m T_{opt} IC (b) 100 m T_{opt} at 0.25 d (c) 100 m T_{opt} at 20 d

(d) 100 m $\Delta_{opt}T_{avg} = T_{avg} - T_{opt}$ IC (e) 100 m $\Delta_{opt}T_{avg}$ at 0.25 d (f) 100 m $\Delta_{opt}T_{avg}$ at 20 d

(g) 100 m $\Delta_{opt}T_{spin-up1}$ IC (h) 100 m $\Delta_{opt}T_{spin-up1}$ at 0.25 d (i) 100 m $\Delta_{opt}T_{spin-up1}$ at 20 d

(j) 100 m $\Delta_{opt}T_{spin-up2}$ IC (k) 100 m $\Delta_{opt}T_{spin-up2}$ at 0.25 d (l) 100 m $\Delta_{opt}T_{spin-up2}$ at 20 d

Fig. 7. As for Fig. 6, but comparing the 100 m temperature fields. Results include: adjustment differences between hindcasts with optimized and averaged ICs appear by 0.25 day off northern coast of Taiwan and advect into Kuroshio; much larger differences 1–2 °C between optimized and spin-up hindcasts. Errors continue to grow throughout the 20 simulation days.

second allowing the tracers to vary during the spin-up but nudged to their ICs at the boundaries (Fig. 5(d)). Both the optimized IC and the IC using averaged $\Psi_{C^{iu}}$ (Fig. 5(a) and (b)) show a defined Kuroshio current. The spin-up ICs after 12.5 days of adjustment do not show nearly as well-defined Kuroshio currents, even though their KEs have stabilized by then (Fig. 5(e)). Also shown in Fig. 5(e) are the KE from the unforced simulations from the reduced physics ICs. The optimized and averaged $\Psi_{C^{iu}}$ ICs show a much more uniform KE history over the simulation, indicating that the reduced physics ICs were near one attracting dynamic equilibria of the PE

dynamics for that region and period. The spin-up solutions have KEs with large oscillations for a long duration before settling into different attracting regime (with larger KE). The larger KE in spin-up solutions are reflected in over estimates of currents and eddies away from the Kuroshio. That a nonlinear PE model can have multiple (dynamic) equilibria should come as no surprise, even relatively simple nonlinear systems can have multiple equilibria (Dijkstra and Katsman, 1997; Simonnet et al., 2009; Sapsis et al., 2013).

Forced hindcast simulations, starting from 5 Aug 2009, from these ICs were made using the MSEAS PE model (Appendix A and HL10) with atmospheric fluxes from NOGAPS and barotropic tides created using Logutov and Lermusiaux (2008) with boundary forcing from OTIS (Egbert and Erofeeva, 2002). Fig. 6 shows the 100 m velocities from these simulations. After 20 days, the simulations from the reduced physics ICs (Fig. 6(c) and (e)) maintain defined Kuroshio currents and develop a loop branch into the strait of Luzon. The spin-up from frozen tracers develops a better defined Kuroshio in the interior but not at the inflow and outflow boundaries of the domain (Fig. 6(i)). The Kuroshio in the spin-up from nudged tracers loses coherency (Fig. 6(l)). Fig. 7 shows a comparison of the 100 m temperature between these hindcasts. The 100 m T of the simulation from optimized ICs is shown in Fig. 7(a)–(c). Differences between 100 m T from the run using averaged $\Psi_{C^{iu}}$ ICs with the 100 m T from the run using optimized ICs are in Fig. 7(d)–(f). Larger (0.25 °C) differences appear in initial adjustment (0.25 d, Fig. 7(e)) off the NE coast of Taiwan. These differences advect off Taiwan and lead to differences in the Kuroshio of 0.1–0.2 ° C. The simulations from spin-up ICs showed larger differences, 1 °C for the spin-up from "frozen" tracers (Fig. 7(g)–(i)) and 1–2 °C for the spin-up in which tracers were allowed to vary (Fig. 7(j)–(l)). These differences grew throughout the 20 day simulation.

We compare the hindcasts to independent T data from sea gliders (Gawarkiewicz et al., 2011) repositioned in the Kuroshio off the coast of Taiwan (Fig. 8(a) and (b)) during 19–22 August 2009, 2 weeks into the simulations. Temperature RMS errors (averaged along the glider tracks, Fig. 8(c)) show that the hindcasts from the optimized and averaged $\Psi_{C^{iu}}$ ICs have significantly smaller errors than did the hindcasts from spin-up ICs. Along-track temperature differences between the hindcasts from optimized ICs and the glider data are shown in Fig. 8(d). Similar difference sections are shown for the other hindcasts (Fig. 8(e)–(g)), but only where these differences exceed the differences in the optimized run. The optimized ICs are better than all other simulations almost everywhere.

4.3. Philippine Archipelago

For further evaluation of our methodology, we turn to the Philippine Archipelago region during February 2–March 20, 2009, as part of the Philippine Straits Dynamics Experiment (PhilEx; Gordon and Villanoy, 2011; Lermusiaux et al., 2011). We consider a 1656 × 1503 km domain (Fig. 9) that is discretized with 9 km horizontal resolution and 70 vertical levels in a generalized coordinate system. The resulting geometry is complex, with 30 interior islands, 2 exterior coasts and numerous straits. A 2 Feb 2009 initialization is created using the February WOA05 climatology (Locarnini et al., 2006; Antonov et al., 2006) mapped with the FMM-based OA (Agarwal and Lermusiaux, 2011). The $\vec{u}_{(0)}$ is constructed using a combination of (i) velocities in geostrophic balance with a 1000 m LNM, (ii) velocity anomalies derived from SSH anomaly (CCAR; Leben et al., 2002) using Eq. (21) vertically extended with a 400 m Gaussian decay scale, (iii) feature model velocities for the bottom currents through the Mindoro (12N, 120.75E) and Dipolog (9N, 123E) Straits, and, (iv) at the open boundaries, transports from the HYbrid Coordinate Ocean Model (HYCOM; Bleck, 2002; Hurlburt et al., 2011). When using feature models for straits, care is needed to ensure the transports enter and exit through $\partial\mathcal{D}$, rather than close in the interior of $\mathcal{D}$. Based on literature estimates the flow originated a mid-level jet in the South China Sea (SCS; 15N, 120E) and broadly exited the domain in the Mindanao current in the Pacific (7N, 123E). To model this we added a feature model jet in the SCS and a boundary outflow velocity in the Pacific:

$$u_{FM} = u_{Mindoro} + u_{Dipolog} + u_{SCS} + u_{boundary\ outflow}$$

and use Eq. (5) to smoothly join the pieces. The HYCOM transports are divided by bathymetry of our modeling domain to produce barotropic velocities, which are then added to the velocities from (i)–(iii) at the open boundaries of the modeling domain. This procedure puts the HYCOM transports directly into Ψ_{b^e} (Eq. (10)) and uses the optimizing Eq. (5) to extend these boundary transports into the interior, consistent with our bathymetry and coastlines. Applying the simple bathymetry constraints leads to $\vec{u}_{(0)}$. Following with the level-by-level coastal constraints results in $\vec{u}_{(1)}$, which is interpolated to generalized coordinates and used to construct $H\vec{U}_{(0)}$ (Eq. (1)).

We start by comparing in Fig. (9) the fields Ψ and $\vec{U}_{(1)}$ estimated using island values, $\Psi_{C^{iu}}$, obtained by our optimization (Eq. (15)) to those estimated using $\Psi_{C^{iu}}$ obtained by averaging of $\Psi_{(0)}$ along the islands (Eq. (13)). In the broad strokes, the solution obtained from averaging (Fig. 9(b) and (d)) agrees with that obtained from the optimization (Fig. 9(a) and (c)). This can be attributed to the constraints imposed by the SSH and HYCOM transports on the overall solution and by bathymetry constraints on the currents (e.g. the Northern Equatorial Current, NEC, which has already split into northern and southern branches by the time it enters the eastern boundary of our domain, remains east of the archipelago, following the Philippines escarpment). However, looking at differences (Fig. 9(b) and (d)), we see significant updates in how currents circulate the Archipelago in the two solutions. The solution obtained from averaged $\Psi_{C^{iu}}$ suffers from over estimates of the sub-tidal transports in many of the straits (near the northern end of the island of Palawan (12N, 120E); in the Balabac Strait (7N, 117E), Surigao Strait (10.5 N, 126E), Sibutu Strait (5N, 120E) and Zamboanga Strait (5N, 122E); and between the islands of Panay and Negros (12N, 123E)): peak barotropic velocities reach 110 cm/s. The solution obtained using optimized $\Psi_{C^{iu}}$ reduces the peak barotropic velocity to 48 cm/s (around Borneo (5N, 119E), eastern Sulu Archipelago (6N, 122E) and northern end of Palawan).

4.3.1. Optimization weights and velocity limits

We now consider the effects of different choices for the weights (ϖ^{uu}_{nm}, ϖ^{uc}_{nk} and ϖ^{uo}_{nb}) in the island optimization as well as the effects of including velocity limits. In Fig. 9(c), we presented $\vec{U}_{(1)}$ computed using $\Psi_{C^{iu}}$ obtained by our optimization with weights equal to the reciprocal of the square of the minimum cross-sectional area between the islands obtained via FMM, i.e. $\varpi^{uu}_{nm} = (\mathcal{A}_{global\ min}/\mathcal{A}_{nm})^2$, similarly for ϖ^{uc}_{nk} and ϖ^{uo}_{nb}. To this, we compare the $\vec{U}_{(1)}$ computed using $\Psi_{C^{iu}}$ obtained by our optimization but weighted by the squared-reciprocal of the minimum Euclidean distance (d^2_{Enm}) between the islands, i.e. $\varpi^{uu}_{nm} = (d_{Eglobal\ min}/d_{nm})^2$, similarly for ϖ^{uc}_{nk} and ϖ^{uo}_{nb} and weighted by the squared reciprocal of the minimum in-water distance computed by FMM, i.e. $\varpi^{uu}_{nm} = (d_{global\ min}/d_{nm})^2$, similarly for ϖ^{uc}_{nk} and ϖ^{uo}_{nb}. Both distance weightings produce very similar currents to each other and increase the peak barotropic velocity to 58 cm/s. This strong similarity between the two

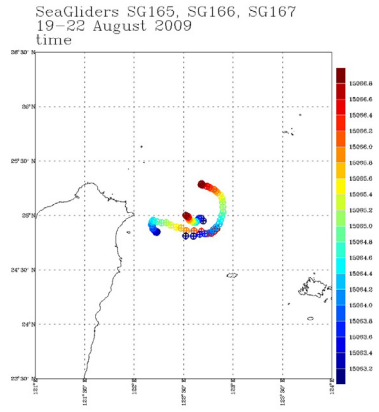

(a) Sea glider positions colored by time

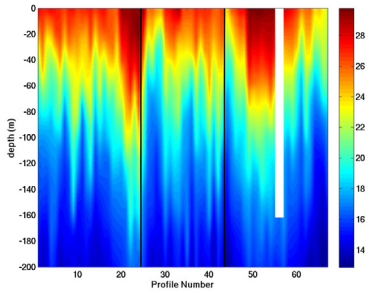

(b) Glider T data cross sections along SG165, SG166, SG167 (separated by black lines)

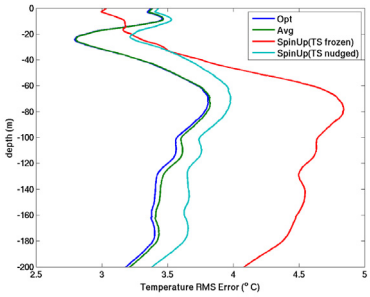

(c) RMS T errors for 4 hindcasts

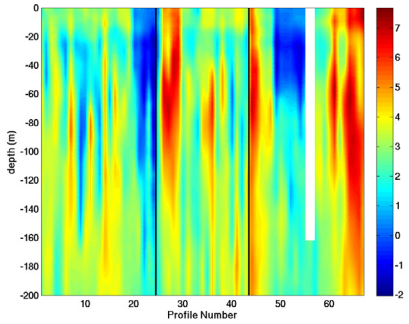

(d) $\Delta T_{opt} = T_{opt} - T_{data}$

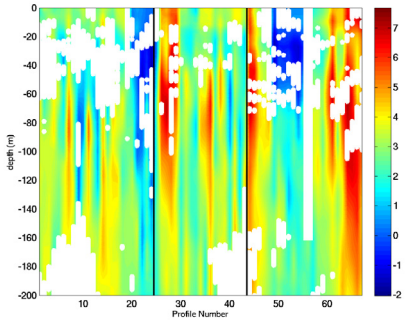

(e) ΔT_{avg} where $|\Delta T_{avg}| > |\Delta T_{opt}|$

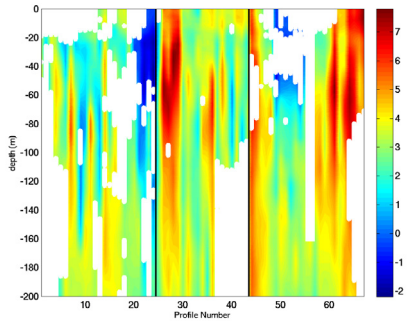

(f) $\Delta T_{spin-up1}$ where $|\Delta T_{spin-up1}| > |\Delta T_{opt}|$

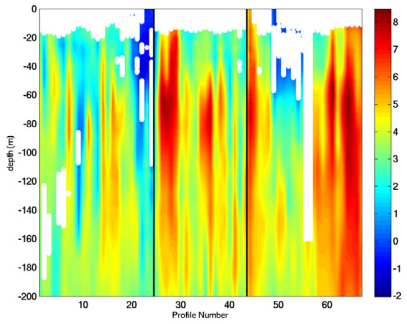

(g) $\Delta T_{spin-up2}$ where $|\Delta T_{spin-up2}| > |\Delta T_{opt}|$

Fig. 8. Comparing temperature from the 4 hindcasts shown on Figs. 6 and 7 to independent in situ data from 3 Sea Gliders at 2 weeks into the simulations. (a) and (b) Glider positions and data. (c) Along-track RMS errors for 4 hindcasts. (d)–(g) Along-track temperature differences for 4 hindcasts. For last 3 hindcasts, differences are shown only where they are larger than the differences of the hindcast from our optimized ICs. This hindcast shows best match to data, on average and almost everywhere.

distance-weighted solutions is because the two distance measures are the same for neighboring islands (with the largest weights) while they generally differ most for the widest separated islands (with the least weight). To see the updates between these two distance-weighted solutions and the area weighted solution, we consider the two difference fields (Fig. 10(a) and (b)). The largest updates are in the Sibutu Strait, Balabac Strait, Visayan sea (11N, 123E) and Surigao Strait.

We illustrate the velocity limiting option by limiting the target transports between islands and coasts with a maximum *average* barotropic velocity of 5 cm/s. The resulting solution slightly reduced the peak barotropic velocity to 44 cm/s. The differences between the solutions with and without velocity limiting (Fig. 10(c)) show that the largest differences are in the Sibutu Strait, Balabac Strait, northern Sibuyan sea (13N, 122E), Surigao Strait and eastern Sulu Archipelago.

4.3.2. Imposing inter-island transports

We now utilize and illustrate our optimization method (Table 2) but turning on the option of imposing externally obtained transports between pairs of islands, Eq. (17). Specifically, Gordon et al. (2011) estimate mean westward transports through the Dipolog (9N, 123E) and Surigao (10.5N, 126E) Straits of 0.5 Sv and 0.3 Sv, respectively, using moorings (15 months deployment, Jan

2008–Mar 2009) and ADCP from several cruises (Jun 2007, Jan 2008 and Mar 2009). For the much smaller subset period 2 Feb–25 Mar 2009, Lermusiaux et al., 2011 estimate a mean 0.77 Sv westward transport through Dipolog with a 1.4 Sv standard deviation (Fig. 7e). During 2–8 Feb 2009, they find that the mean transport through Dipolog is reversed (mean eastward transport of 0.7 Sv and an initial eastward transport of 1.1 Sv) in response to the northeast monsoon (May et al., 2011). Hence we choose here as an extreme test to impose the Gordon et al. (2011) 15-month-average transports in an updated Feb 2 initialization. Of course, these 15-month averages are not expected to be accurate for the single-day 2 Feb 2009 transports, we merely use them as a test of our method: the average and single-day transport estimates are within the variability and so are representative of the kinds of changes the method should be able to handle. The questions we wish to answer are: (a) can the method impose these values? and (b) if so, are the transports through the remaining straits still sensible? For the first question, we ran our optimization with a wide range of weights, shown in Table 3. From this we see that these specific transports can be imposed if the weights are large enough (increase the FMM weights by a factor 100 for Surigao and by a factor of 1000–10000 for Dipolog). To answer the second question, the barotropic velocities resulting from the imposed transports are shown in Fig. 11 for the PhilEx domain previously shown and two nested sub-domains with 3 km resolution. The first is a 552 × 519 km domain covering the Mindoro Strait and the Sibuyan and Visayan seas. The second is a 895 × 303 km domain covering the Bohol Sea (9N, 125E). The number and distribution of generalized vertical levels in both sub-domains is identical to the 9 km domain, although the bathymetry is refined. Even though the transports are reversed through Dipolog and Surigao, the barotropic velocities elsewhere remain sensible (peak values remain less than 50 cm/s in all domains), confirming that such reversal could occur in the real ocean. Looking at the differences between

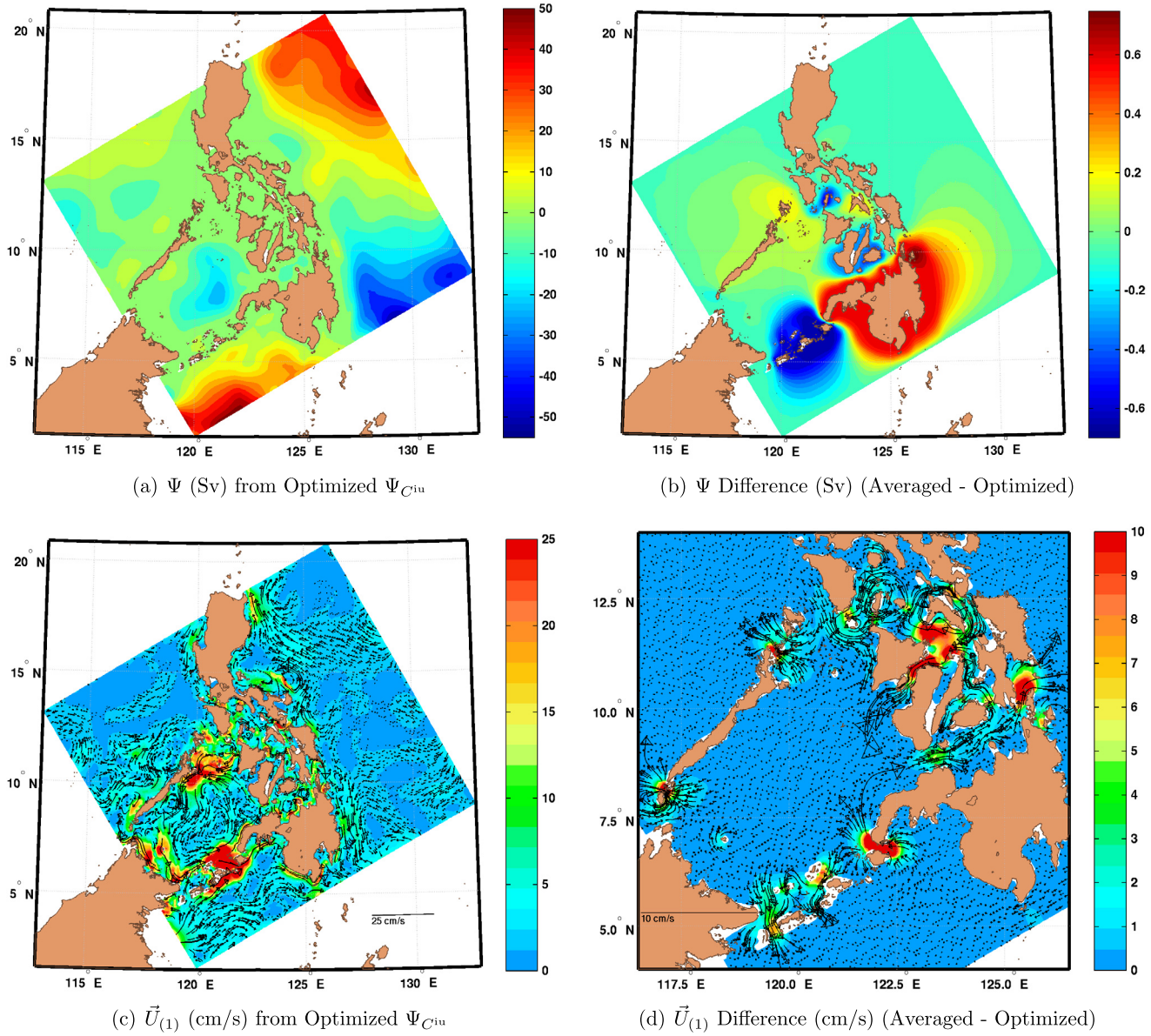

(a) Ψ (Sv) from Optimized $\Psi_{C^{iu}}$

(b) Ψ Difference (Sv) (Averaged - Optimized)

(c) $\vec{U}_{(1)}$ (cm/s) from Optimized $\Psi_{C^{iu}}$

(d) $\vec{U}_{(1)}$ Difference (cm/s) (Averaged - Optimized)

Fig. 9. Philippines Archipelago. Comparison of initializations computed using $\Psi_{C^{iu}}$ obtained via our optimization methodology (Eq. (15)) to those obtained via an averaging method (Eq. (13)). (a) and (b) maps of Ψ. (c) and (d) maps of $\vec{U}_{(1)}$ magnitudes overlaid with vectors. (Note (d) is a zoom of the regions with the largest differences.) Optimizing island values removes excessive transports in various straits.

the solution with and without imposed transports (Fig. 11(b)), we see the changes are as expected. The flows are reversed in the two straits as imposed. The imposition of a larger transport through Dipolog than Surigao draws additional transport through the San Bernadino strait (12N, 124E) and the Visayan Sea. The added transport through Dipolog into the Sulu Sea (7.5N, 120E) exits through the Sulu Archipelago. Elsewhere the changes are negligible.

4.3.3. Nesting strategies

We now exemplify our optimized initialization for use in nested multi-resolution simulations (HL10). To ensure consistency between a coarse and fine solution, we obtain the BCs at the outer boundary of the fine domain by interpolation from the coarse domain solution (i.e. we by-pass Eq. (10) the "Construct Exterior

Table 3
Testing weights for imposing inter-island transports. Our island optimization scheme is employed with the imposition of inter-island transports, Eq. (17). Here, we impose westward transports of 0.5 Sv through the Dipolog Strait and 0.3 Sv through the Surigao Strait. The resulting transports from calculations using different weights are compared to the default values, $\varpi^{uu}_{nm} = (\mathcal{A}_{global\ min}/\mathcal{A}_{nm})^2$. For Dipolog $\varpi^{uu}_{nm} = 2.19 \times 10^{-3}$ while for Surigao $\varpi^{uu}_{nm} = 2.29 \times 10^{-2}$.

Weights for imposing inter-island transports	Westward transports (Sv)	
	Dipolog	Surigao
$--$	−1.1	−0.63
ϖ^{uu}_{nm}	−0.60	−0.20
$10\ \varpi^{uu}_{nm}$	−0.18	0.26
$100\ \varpi^{uu}_{nm}$	0.34	0.30
$1000\ \varpi^{uu}_{nm}$	0.48	0.30
$10000\ \varpi^{uu}_{nm}$	0.50	0.30

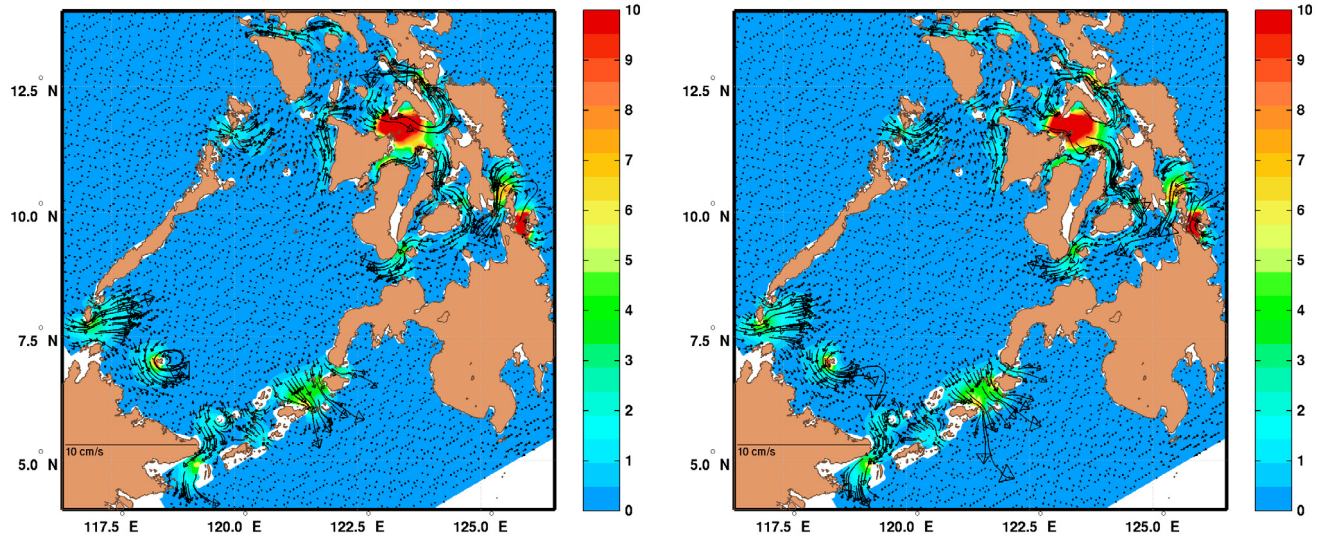

(a) $\vec{U}_{(1)}$ difference
Euclidean $(d_{Eglobal\ min}/d_{Enm})^2$ - FMM $(\mathcal{A}_{global\ min}/\mathcal{A}_{nm})^2$

(b) $\vec{U}_{(1)}$ difference
FMM $(d_{global\ min}/d_{nm})^2$ - FMM $(\mathcal{A}_{global\ min}/\mathcal{A}_{nm})^2$

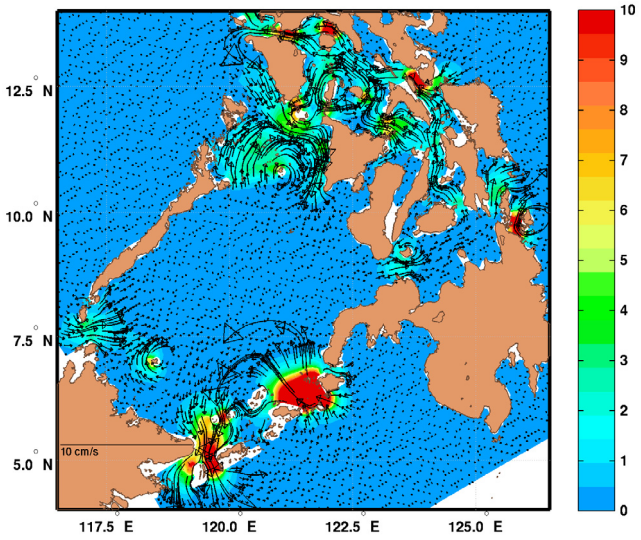

(c) $\vec{U}_{(1)}$ difference
FMM $(\mathcal{A}_{global\ min}/\mathcal{A}_{nm})^2$ (velocity limit - no limit)

Fig. 10. Differences between $\vec{U}_{(1)}$ constructed using three weighting schemes in the Philippines and the reference result using our FMM $\varpi^{uu}_{nm} = (\mathcal{A}_{global\ min}/\mathcal{A}_{nm})^2$ (shown on Fig. 9(c)); maps of magnitudes overlaid with vectors, restricted to the region of the largest differences. Our FMM area weightings reduces spurious large velocities in various straits. Adding velocity limiting further reduces the velocities in especially problematic straits.

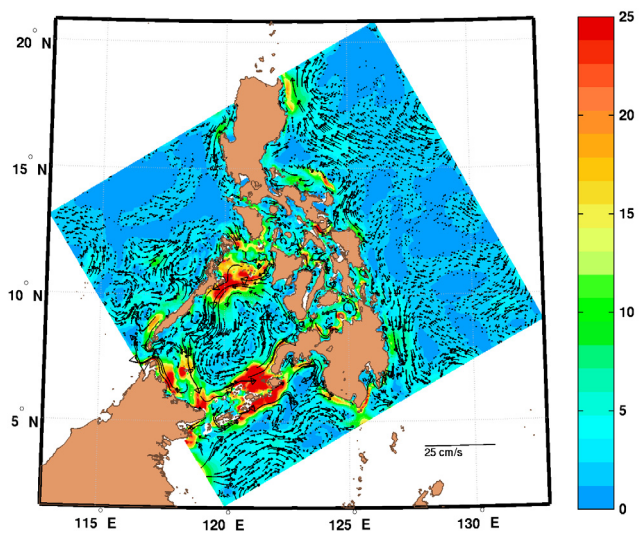

(a) $\vec{U}_{(1)}$ (cm/s) in 9 km domain for the Philippine Archipelago

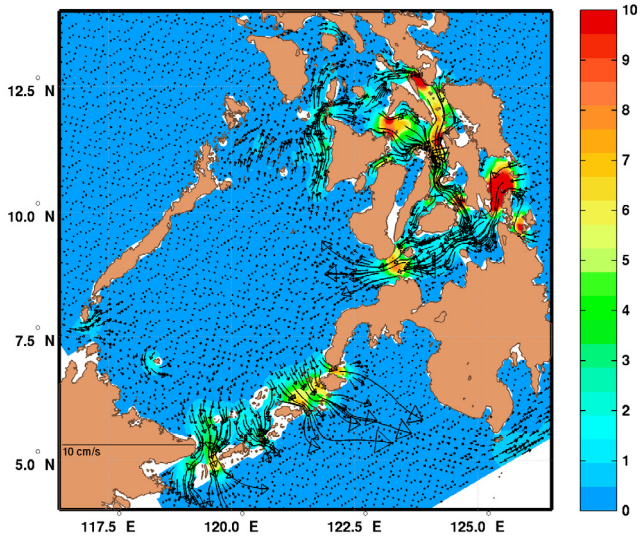

(b) $\vec{U}_{(1)}$ (cm/s) difference (imposed - not imposed). Only showing region of large differences

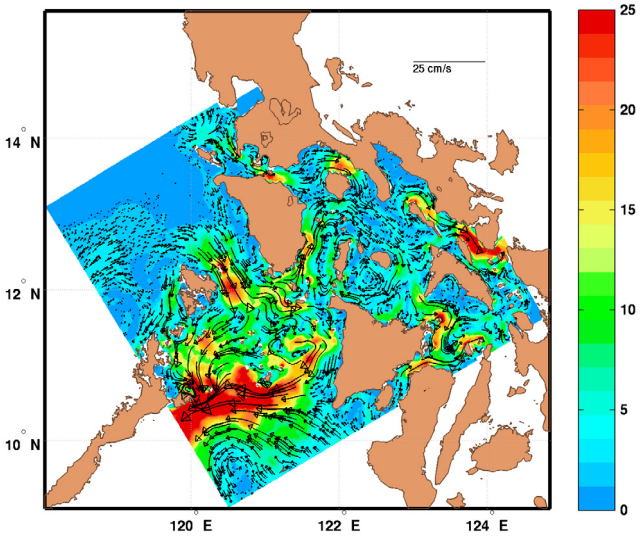

(c) $\vec{U}_{(1)}$ (cm/s) in 3 km domain for Mindoro Strait

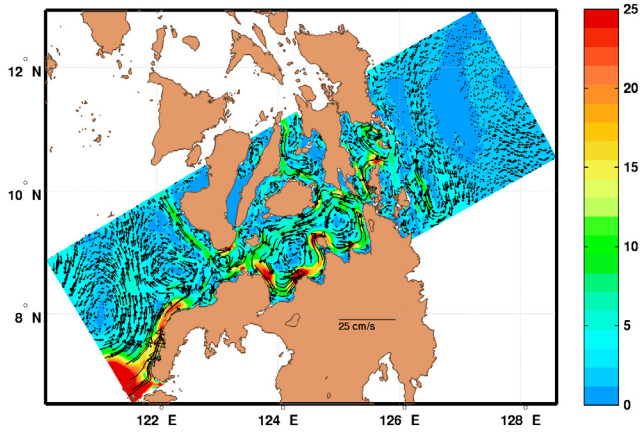

(d) $\vec{U}_{(1)}$ (cm/s) in 3 km domain for Bohol Sea

Fig. 11. $\vec{U}_{(1)}$ after imposing transports of 0.5 Sv through Dipolog Strait (9 N,123E) and 0.3 Sv through Surigao Strait (10.5 N,126E), maps of $\vec{U}_{(1)}$ magnitudes overlaid with $\vec{U}_{(1)}$ vectors. Using the maximum weights of Table 3, the desired transports are imposed, resulting in the reversal of the transports through these straits. The imposition of a larger transport through Dipolog than Surigao draws additional transport through the San Bernadino strait and the Visayan Sea. The added transport through Dipolog into the Sulu Sea exits through the Sulu Archipelago. Elsewhere the changes are negligible.

BCs" step of Table 2 and instead interpolate the coarse-domain Ψ to obtain the fine domain Ψ_{b^e} values). Here we explore how much of the additional information from the coarse domain (i.e. inter-island transports) should be included in the fine domain solution.

We consider the 3 km Mindoro Strait domain nested within our larger 9 km domain. In Fig. 12, we zoom in on the southeast portion of our nested sub-domain, encompassing the Sibuyan sea. Fig. 12(a) shows the $\vec{U}_{(1)}$ in the 9 km domain obtained with our optimization scheme (Table 2) including the velocity limiting option with an imposed maximum 80 cm/s target average barotropic velocity. Fig. 12(b) shows the final $\vec{U}_{(1)}$ in the 3 km domain. We compare this final result with a couple of different strategies. The first was to not only use the 9 km solution for BCs, Ψ_{b^e}, at the outer boundary of the 3 km domain, but to also retain the transport streamfunction values along the islands that are also resolved in the larger domain (e.g. Mindoro 13N,121E; Panay 11N,123E). This occurs in two steps (i) these values of Ψ_{C^c} are included in the "certain coast solution" (Eq. (12) and Table 2) and (ii) these islands are included in the set of coastlines with known streamfunction values. The intent is to ensure a greater consistency between the initial coarse and fine domain fields. The difference between this strategy and the final strategy is shown in Fig. 12(d). An unintended consequence of retaining the 9 km island values is an increase in $\vec{U}_{(1)}$ in certain channels due to the increased coastal and bathymetry resolution of the fine domain. In particular, the peak $\vec{U}_{(1)}$ in the Verde Island passage between Mindoro and Luzon (13.5N,121E) increases from 17 cm/s in the coarse domain to 50 cm/s in the fine.

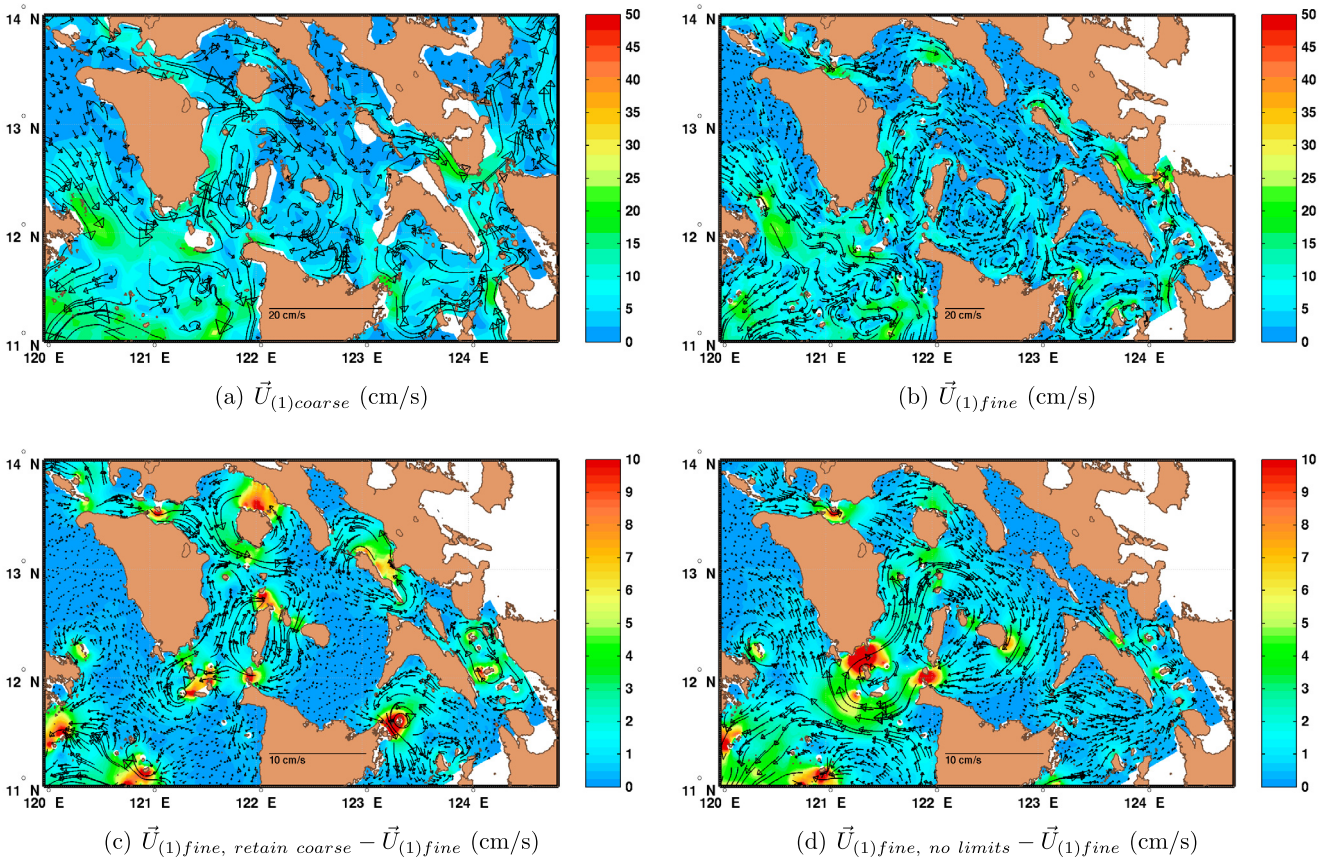

Fig. 12. Testing different strategies for initializing nested sub-domains in the Philippines. Shown are maps the magnitudes of $\vec{U}_{(1)}$ (cm/s) overlaid with $\vec{U}_{(1)}$ vectors. (a) $\vec{U}_{(1)}$ in coarse (9 km) domain. (b) $\vec{U}_{(1)}$ in fine (3 km) domain, in which all island values are recomputed in fine domain using velocity limits (Section 3.2.2). (d) Difference between $\vec{U}_{(1)}$ in fine (3 km) domain retaining island values from coarse domain (for inter-domain consistency) and $\vec{U}_{(1)fine}$. $\vec{U}_{(1)}$ in Verde Island passage (13.5N, 121E) increases from 17 cm/s to 50 cm/s due to reduced cross-section area from refined coasts and bathymetry. (d) Difference between $\vec{U}_{(1)}$ in fine (3 km) domain without imposing velocity limits and $\vec{U}_{(1)fine}$. $\vec{U}_{(1)}$ reduces in Verde Island passage from 50 to 30 cm/s but increases $\vec{U}_{(1)}$ to 30 cm/s at southern tip of Mindoro (12 N,121.25E).

To reduce these velocities, we allow our optimization algorithm to work on all the islands in the fine domain: the streamfunction values on all islands are then assumed uncertain. The OBCs are still obtained by interpolation from the 9 km domain. Fig. 12(d) shows the difference between this strategy and the final one. Optimizing these island values for the fine domain reduces the peak barotropic velocity in the Verde Island passage to 30 cm/s, but increases it to 30 cm/s at the southern tip of Mindoro (12.25N, 121E). When we add velocity limits to the optimization (keeping the interpolated OBCs, our final strategy), we obtain the results shown on Fig. 12(b): the peak barotropic velocities are brought down to 20 cm/s in the Verde Island passage and 10 cm/s at the southern tip of Mindoro. This shows that for nested initialization, our weak-constraint optimization algorithm should be used for all islands, adding local weak velocity bounds as needed. The results are then well adjusted fine domain fields that still match the coarse domain solution at the boundaries of the fine domain.

5. Summary and conclusions

In this manuscript, we derived and applied a methodology for the efficient semi-analytical initialization of 3D velocity and transport fields in coastal regions with multiscale dynamics and complex multiply-connected geometries, including islands and archipelagos. These fields are consistent with the synoptic observations available, geometry, free-surface PE dynamics and any other relevant information to evolve without spurious initial transients. They can be directly used for model initialization or as an improved initial guess for a variational scheme.

Our weighted least squares optimization starts from first-guess sub-tidal velocity fields that satisfy simple bathymetric constraints. To obtain the exact solutions for the first correction velocities which best fit these first-guesses while satisfying no-normal flow into complex coastlines and bathymetry, we derive successive level-by-level (layer-by-layer) Euler–Lagrange equations for the interior, boundary and island streamfunction variables. These new equations are: (i) a Poisson equation for a streamfunction representation of the velocity; (ii) a 1D Poisson equation along the external boundary for the Dirichlet OBCs which best fit the first-guess flow through the open boundaries; and (iii) robust algebraic equations for selecting constant values for the streamfunction along the uncertain islands, best-fitting the first-guess values using weights that are functions of minimum ocean distances or cross sectional areas, both computed by FMM. A second correction is derived for cases where the full 3D dynamics is critical, employing a predictor–corrector algorithm to fit the no-normal flow constraints in 3D. The first guess sub-tidal transport is computed from either the first or second guess velocities as appropriate. A first correction transport is then computed using steps (i)–(iii) derived for transport. Additional information on the transport and velocity fields is also incorporated as weak or strong constraints, including for example specific net transports between coasts or weak upper and lower bounds on the barotropic velocity in specific straits.

We applied our methodology in three regions: (i) around the Hawaiian islands of Kauai/Niihau (ii) the Taiwan/Kuroshio region,

and (iii) in the Philippines Archipelago. In the Hawaiian study, four day simulations from 3 initializations were compared: (i) starting from our optimized ICs (ii) from ICs using averaged $\Psi_{C^{iu}}$ and (iii) from spin-up ICs. If our optimization is not used, both the ICs and the initial adjustment simulations from the ICs over estimate the transport between the islands. Our optimization produced a current which was primarily around Kauai/Niihau rather than between them, in accord with historical observations. The erroneous transports led to large O(1–1.5 °C) differences in temperature. These temperature differences grew as the simulations progressed (i.e. initial velocity errors were transferred to tracer errors). In the Taiwan-Kuroshio region, we compared four initializations and their subsequent evolutions, starting from (i) our optimized ICs, (ii) ICs using averaged $\Psi_{C^{iu}}$, (iii) spin-up with fixed TS and (iv) spin-up allowing TS to vary but nudged to ICs at the open boundaries. Neither of the spin-up ICs led to as well-developed Kuroshio currents as (i) or (ii) did, even after the spin-up KEs grew and stabilized around an erroneous "attractor regime". However, the KEs from the unforced runs of (i) and (ii) showed a KE history quasi-steady at the optimized value. The forced 20-day hindcasts confirmed the advantages of initializing from our optimized velocities, including better representations of the Kuroshio. The quantitative evaluation of these hindcasts by comparison with independent *in situ* data after 2 weeks of simulation showed by far the largest errors in the hindcasts from spin-up while our optimized ICs produced the best match.

The third region was the multiply-connected Philippines Archipelago. The solution obtained from the averaging method suffered from over estimates of the transports in many of the straits while our optimized solution produced realistic peak sub-tidal barotropic velocities. We also evaluated the effects of different weighting functions and showed that using weights based on the minimum cross-sectional areas among islands (computed by FMM) was the most adequate. We tested the effects of including weak upper bounds on velocities and found that optimized results were in accord with the bounds chosen. We also showed that our option of weakly imposing externally obtained transports between pairs of islands could reverse the initial flows through the Dipolog and Surigao Straits if the corresponding weights were strong enough. This example was used to show that transports through these straits could also reverse in reality since their reversals retained sensible velocities and expected currents elsewhere. Finally, we studied our optimized nested initialization schemes to use in multi-resolution simulations. Since the multi-resolution domains have different bathymetries, coastlines, islands, flow features and dynamics, we found that the best approach was to let our optimization algorithm work on all islands and flows between islands, only imposing the cross-scale information as strong constraints on the boundary and applying weak bounds on the average barotropic velocity where needed. The result is then well adjusted multi-resolution initial velocity fields, consistent at all scales within and across the nested domains.

We have found that our optimization, particularly the weak constraint towards the minimum inter-island transport that is in accord with the first-guess velocities (Eq. (15)), provides important velocity corrections in complex archipelagos. This was found to be critical where the available data did not resolve the bathymetric/coastal effects. The velocity corrections from our methodology optimized the kinetic energy locally, eliminating unrealistic hotspots, while respecting continuity constraints and the boundary conditions for multiple islands and tortuous coastlines. When optimizing transports, weighting functions that lead to the minimization of barotropic velocity differences are found to be more robust and to better control velocities than those that lead to the minimization of transport differences. In all of the examples shown, it is key to realize that in complex domains without our optimization, the initial fields were too erroneous and unbalanced. We confirmed that such errors can damage predictions for future times.

For the future, there are many opportunities for refinement and application of our methodology. For the refinements, even though our approach is independent of the discretization employed, other discretizations (Deleersnijder et al., 2010; Ueckermann and Lermusiaux, 2010; Lermusiaux et al., 2013) may have specific challenges. Different weighting and cost functions can be researched, for example specific functions for non-hydrostatic flow initialization. Considering applications to other regions and dynamics, a promising example is the downscaling of climate predictions to initialize simulations in complex coastal regions, including sea-level change implications. Real-time optimized initialization for rapid responses operations to specific events or for other societal applications are useful directions. Finally, ocean ecosystem initialization (Beşiktepe et al., 2003) as well as other multi-model and multi-dynamics applications should be further investigated.

Acknowledgments

We are grateful to the Office of Naval Research for research support under Grants N00014-08-1-109 (ONR6.1), N00014-08-1-0680 (PLUS-INP), N00014-08-1-0586 (QPE), N00014-07-1-0473 (PhilEx), N00014-09-1-0676 (Autonomy), N00014-11-1-0701 (MURI-IODA), N00014-12-1-0944 (ONR6.2) and N00014-13-1-0518 (Multi-DA), and to the Naval Research Laboratory for research support under Grant N00173-13-2-C009 to the Massachusetts Institute of Technology. We are thankful to Wayne G. Leslie, Carlos Lozano and to the MSEAS group for useful inputs and discussions. We are grateful to the QPE, PLUS-INP and PhilEx teams for their fruitful collaborations. We thank C. Lee for providing sea glider data and B. Leben and CCAR for providing SSH anomaly data. We thank the three anonymous reviewers and the associate editor for their useful suggestions.

Appendix A. Ocean modeling primitive equations and the MSEAS modeling system

Free-surface primitive equations (PEs). The equations are derived from the Navier–Stokes equations and first law of thermodynamics and conservation of salt, under the Boussinesq, thin-layer and hydrostatic approximations (e.g. Cushman-Roisin and Beckers, 2010). They consist of,

$$\text{Cons. Mass} \quad \nabla\cdot\vec{u}+\frac{\partial w}{\partial z}=0, \tag{A.1}$$

$$\text{Cons. Horiz. Mom.} \quad \frac{D\vec{u}}{Dt}+f\hat{k}\times\vec{u}=-\frac{1}{\rho_0}\nabla p+\vec{F}, \tag{A.2}$$

$$\text{Cons. Vert. Mom.} \quad \frac{\partial p}{\partial z}=-\rho g, \tag{A.3}$$

$$\text{Cons. Heat} \quad \frac{DT}{Dt}=F^T, \tag{A.4}$$

$$\text{Cons. Salt} \quad \frac{DS}{Dt}=F^S, \tag{A.5}$$

$$\text{Eq. of State} \quad \rho=\rho(z,T,S), \tag{A.6}$$

$$\text{Free Surface} \quad \frac{\partial\eta}{\partial t}+\nabla\cdot\left(\int_{-H}^{\eta}\vec{u}\,dz\right)=0 \tag{A.7}$$

where: $(\vec{u},w)$ are horizontal and vertical components of velocity; (x,y,z) spatial positions; t time; T temperature; S salinity; $\frac{D}{Dt}$ three-dimensional material derivative; p pressure; f Coriolis parameter; ρ density, ρ_0 (constant) density from a reference state; g acceleration due to gravity; η surface elevation, $H=H(x,y)$ local

water depth in the undisturbed ocean; and, $\hat{k}$ unit direction vector in the vertical direction. The gradient operators, ∇, in Eqs. (A.1) and (A.2) are two dimensional (horizontal) operators. The turbulent sub-gridscale processes are represented by $\vec{F}$, F^T and F^S.

MSEAS modeling system. The above equations are numerically integrated using the finite-volume structured ocean model (HL10) of the Multidisciplinary Simulation, Estimation and Assimilation System (MSEASgroup, 2010). MSEAS is used to study and quantify tidal-to-mesoscale processes over regional domains with complex geometries and varied interactions. Modeling capabilities include implicit two-way nesting for multiscale hydrostatic PE dynamics with a nonlinear free-surface (HL10) and a high-order finite element code on unstructured grids for non-hydrostatic processes also with a nonlinear free-surface (Ueckermann and Lermusiaux, 2010, 2015). Other MSEAS subsystems include: initialization schemes, nested data-assimilative tidal prediction and inversion (Logutov and Lermusiaux, 2008); fast-marching coastal objective analysis (Agarwal and Lermusiaux, 2011); stochastic subgrid-scale models (e.g., Lermusiaux, 2006; Phadnis, 2013); generalized adaptable biogeochemical modeling system; Lagrangian Coherent Structures; non-Gaussian data assimilation and adaptive sampling (Sondergaard and Lermusiaux, 2013a,b; Lermusiaux, 2007); dynamically-orthogonal equations for uncertainty predictions (Sapsis and Lermusiaux, 2009, 2012; Ueckermann et al., 2013); and machine learning of model formulations. The MSEAS software is used for basic and fundamental research and for realistic simulations and predictions in varied regions of the world's ocean (Leslie et al., 2008; Onken et al., 2008; Haley et al., 2009; Gangopadhyay et al., 2011; Ramp et al., 2011; Colin et al., 2013), including monitoring (Lermusiaux et al., 2007), naval exercises including real-time acoustic-ocean predictions (Xu et al., 2008) and environmental management (Cossarini et al., 2009).

Appendix B. Retaining vertical velocity for 3D effects and more complicated bathymetry constraints

In this appendix, we deal with cases in which desired velocity properties are fully 3D, including both horizontal and vertical components (e.g. velocities from a dynamical simulation with its own 3D balance, feature models for flows over sills, geostrophic-Ekman balance with bottom interaction) and are of sufficient resolution to contain meaningful estimates of $w_{(0)}$. For hydrostatic PEs, this vertical velocity comes in through the 2D divergence of the horizontal velocity. However, in Section 3 the algorithms obtained for fitting the 3D velocities and horizontal transports to the geometry enforce a layer-by-layer 2D non-divergence in the chosen vertical discretization. (For non-hydrostatic PEs, one still desires ICs which satisfy continuity.) Hence we now derive a predictor/corrector method to recover the non-zero 2D divergence of the horizontal velocities when that divergence contains a sufficiently meaningful estimate of $w_{(0)}$. The predictor is the first correction velocity estimate, $\vec{u}_{(1)}$, that satisfies the 2D level-by-level constraints. The corrector is a velocity correction, $\Delta\vec{u}$, to recover the nonzero 2D divergences. $\Delta\vec{u}$ best fits the difference $\vec{u}_{(1)} - \vec{u}_{(0)}$ under the no-normal flow constraint in 3D (thereby recovering $w_{(0)}$ via vertical integration of continuity equation (A.2)). The result is the second correction velocity, $\vec{u}_{(2)} = \vec{u}_{(1)} + \Delta\vec{u}$ which recovers the first guess vertical velocity, $\nabla \cdot \vec{u}_{(2)} \approx -\frac{\partial w_{(0)}}{\partial z}$, subject to constraints.

Let $\vec{u}_{(2)}$ be the second correction velocity which best fits the first-guess velocity, $\vec{u}_{(0)}$, while satisfying no-normal flow and retaining the non-zero 2D divergence. By the Helmholtz decomposition, $\vec{u}_{(2)}$ can be written as

$$\vec{u}_{(2)} = \left(\hat{k} \times \nabla\psi\right) + \nabla\phi \tag{B.1}$$

where ψ is a level-by-level streamfunction and ϕ is a level-by-level velocity potential. $\vec{u}_{(1)}$ best fits $\vec{u}_{(0)}$ while satisfying no-normal flow and

$$\vec{u}_{(1)} = \hat{k} \times \nabla\psi$$

We choose $\vec{u}_{(1)}$ as the predictor for $\vec{u}_{(2)}$ and define the corrector, $\Delta\vec{u}$, as

$$\begin{aligned} \Delta\vec{u} &= \vec{u}_{(2)} - \vec{u}_{(1)} \\ &= \nabla\phi \end{aligned} \tag{B.2}$$

Then, defining

$$\Delta\vec{u}_{(0)} = \vec{u}_{(0)} - \vec{u}_{(1)} \tag{B.3}$$

the weighted least squares cost function, J_{div}, to recover the divergence is

$$\begin{aligned} J_{div}(\Delta\tilde{\vec{u}}) &= \frac{1}{2}\iint_{\mathcal{D}} \omega_\phi \left\| \Delta\tilde{\vec{u}} - \Delta\vec{u}_{(0)} \right\|^2 da \\ \Longleftrightarrow J_{div}(\tilde{\phi}) &= \frac{1}{2}\iint_{\mathcal{D}} \omega_\phi \left\| \nabla\tilde{\phi} - \Delta\vec{u}_{(0)} \right\|^2 da \end{aligned} \tag{B.4}$$

where $\Delta\tilde{\vec{u}}$ is any test velocity corrector, $\tilde{\phi}$ the corresponding test velocity potential, ω_ϕ a positive definite weighting function and da an area element. To find the ϕ that minimizes J_{div}, variational calculus is employed:

$$\begin{aligned} J_{div}(\phi + \delta\phi) = J_{div}(\phi) &+ \frac{1}{2}\iint_{\mathcal{D}} \omega_\phi \|\nabla(\delta\phi)\|^2 da - \iint_{\mathcal{D}} \delta\phi \nabla \\ &\cdot \left[\omega_\phi (\nabla\phi - \Delta\vec{u}_{(0)})\right] da \\ &+ \oint_{\partial\mathcal{D}} \omega_\phi \delta\phi (\nabla\phi - \Delta\vec{u}_{(0)}) \cdot \hat{n}\, ds \end{aligned} \tag{B.5}$$

The potential ϕ will minimize J_{div} provided the second and third integrals in Eq. (B.5) are zero. Applying the fundamental theorem of variational calculus, these integrals will be identically zero for ϕ satisfying

$$\nabla \cdot (\omega_\phi \nabla\phi) = \nabla \cdot (\omega_\phi \Delta\vec{u}_{(0)}) \tag{B.6}$$

$$\nabla\phi \cdot \hat{n}|_{\partial\mathcal{D}} = \Delta\vec{u}_{(0)} \cdot \hat{n}|_{\partial\mathcal{D}} \tag{B.7}$$

To enforce no flow through coasts, $\Delta\vec{u}_{(0,np)}$ is defined as

$$\begin{aligned} &\Delta\vec{u}_{(0,np)} \cdot \hat{n}|_{coasts} = 0 \\ &\Delta\vec{u}_{(0,np)} \cdot \hat{t}|_{coasts} = \Delta\vec{u}_{(0)} \cdot \hat{t}|_{coasts} \\ &\Delta\vec{u}_{(0,np)} = \Delta\vec{u}_{(0)} \quad \text{elsewhere} \end{aligned} \tag{B.8}$$

where $\hat{t}$ is the unit tangent. Replacing $\Delta\vec{u}_{(0)}$ with $\Delta\vec{u}_{(0,np)}$ in (B.7) results in

$$\nabla\phi \cdot \hat{n}|_{\partial\mathcal{D}} = \Delta\vec{u}_{(0,np)} \cdot \hat{n}|_{\partial\mathcal{D}} \tag{B.9}$$

As a check on the consistency of using (B.9) with (B.6), Eq. (B.6) is integrated over the domain, followed by an application of the divergence theorem, and a substitution from (B.9). The result is the solvability condition

$$\oint_{\partial\mathcal{D}} \omega_\phi \Delta\vec{u}_{(0,np)} \cdot \hat{n}\, ds = \oint_{\partial\mathcal{D}} \omega_\phi \Delta\vec{u}_{(0)} \cdot \hat{n}\, ds \tag{B.10}$$

Along the open boundaries, $\Delta\vec{u}_{(0)} = \Delta\vec{u}_{(0,np)}$ while along the coasts $\Delta\vec{u}_{(0,np)} \cdot \hat{n}$ is zero. Therefore, Eq. (B.10) reduces to

$$\int_{coasts} \omega_\phi \Delta\vec{u}_{(0)} \cdot \hat{n}\, ds = 0 \tag{B.11}$$

In general Eq. (B.11) is not satisfied. Therefore a "no net normal flow" target velocity correction, $\Delta\vec{u}_{(0,nnp)}$ is sought which best fits $\Delta\vec{u}_{(0)}$ while satisfying (B.11). The least squares cost function J_{nnp} to fit $\Delta\vec{u}_{(0,nnp)}$ is

$$J_{nnp}(\Delta\vec{u}_{(0,nnp)};\lambda) = \int_{coasts} \omega_\phi \left(\Delta\vec{u}_{(0,nnp)}\cdot\hat{n} - \Delta\vec{u}_{(0)}\cdot\hat{n}\right)^2 ds + \lambda\int_{coasts}\omega_\phi\Delta\vec{u}_{(0,nnp)}\cdot\hat{n}\,ds \tag{B.12}$$

where λ is a Lagrange multiplier. To minimize Eq. (B.12) we take derivatives of J_{nnp} with respect to $\Delta\vec{u}_{(0,nnp)}$ and λ and set them equal to zero:

$$\frac{\partial J_{nnp}}{\partial\Delta\vec{u}_{(0,nnp)}} = \omega_\phi\left(\Delta\vec{u}_{(0,nnp)}\cdot\hat{n} - \Delta\vec{u}_{(0)}\cdot\hat{n}\right) + \omega_\phi\lambda = 0$$
$$\frac{\partial J_{nnp}}{\partial\lambda} = \int_{coasts}\omega_\phi\Delta\vec{u}_{(0,nnp)}\cdot\hat{n}\,ds = 0 \tag{B.13}$$

Solving the resulting system yields:

$$\Delta\vec{u}_{(0,nnp)}\cdot\hat{n}\big|_{coasts} = \Delta\vec{u}_{(0)}\cdot\hat{n}\big|_{coasts} - \frac{\int_{coasts}\omega_\phi\Delta\vec{u}_{(0)}\cdot\hat{n}\,ds}{\int_{coasts}\omega_\phi\,ds} \tag{B.14}$$
$$\Delta\vec{u}_{(0,nnp)}\cdot\hat{t}\big|_{coasts} = \Delta\vec{u}_{(0)}\cdot\hat{t}\big|_{coasts}$$
$$\Delta\vec{u}_{(0,nnp)} = \Delta\vec{u}_{(0)} \quad \text{elsewhere.}$$

Substituting (B.14) in (B.6), results in the well-posed modified system

$$\nabla\cdot\left(\omega_\phi\nabla\phi\right) = \nabla\cdot\left(\omega_\phi\Delta\vec{u}_{(0,nnp)}\right) \tag{B.15}$$
$$\nabla\phi\cdot\hat{n}\big|_{\partial\mathcal{D}} = \Delta\vec{u}_{(0,np)}\cdot\hat{n}\big|_{\partial\mathcal{D}}$$

The level-by-level solutions to (B.15) are substituted into (B.2), and solved for $\vec{u}_{(2)}$, which preserves no-normal flow in the final velocities:

$$\vec{u}_{(2)} = \vec{u}_{(1)} + \nabla\phi \tag{B.16}$$

Appendix C. Free surface and tidal initialization

This appendix summarizes our scheme to create ICs consistent with the free surface and tides in complex domains. Some of this material is in Appendices 2.2 and 2.3 of HL10. Here we expand on details needed for the present work and apply the notation of this manuscript.

C.1. Sub-tidal free surface

Once velocities and transport are constrained for the model geometry, we need a sub-tidal free surface in dynamic balance with them. When initializing from another model output, the free surface should be directly available. When initializing from reduced dynamics, a consistent free surface needs to be constructed. Summarizing Appendix 2.2 of HL10, the reduced dynamical equation, with the free surface contribution made explicit, is integrated in the vertical (HL10 Eq. 67) and the divergence operator is applied to obtain a Poisson equation for $\eta_{(0)}$ (HL10 Eq. 68). Dirichlet OBCs are obtained by a tangential integral of the vertically integrated equation along the open boundaries. Along the coastlines, no-normal flow is enforced by applying zero Neumann conditions. The resulting system of equations is solved for $\eta_{(0)}$. To maintain the transport, the barotropic velocity is rescaled from

$$\vec{U}_{(2)} = \frac{H}{H+\eta_{(0)}}\vec{U}_{(1)} \tag{C.1}$$

If tides are not in initial fields, $\vec{u}'$, $\vec{u}$ and w are constructed using Eqs. (C.4)–(C.6) but with $\eta_{(0)}$, $\vec{U}_{(2)}$ replacing $\eta_{(1)}$, $\vec{U}_{(3)}$ ($\vec{u}$ still respects no-normal flow).

C.2. Tides and other external forcing

The final step of the initialization is to obtain the tidal free surface and velocity, and add both to the sub-tidal fields computed above. Regional barotropic tidal fields are readily available (e.g., Egbert and Erofeeva, 2002, 2013) and if higher spatial resolutions are needed, finer inversions can be used (e.g., Logutov, 2008; Logutov and Lermusiaux, 2008). The barotropic tides, η_{tide} and $\vec{U}_{tide}$, are best-fit to a set of tidal fields under the constraints of satisfying the exact discrete divergence relation of the model geometry and no-normal flow into coasts. The tidal elevations and transports are superimposed with the sub tidal counterparts constructed in Section C.1

$$\eta_{(1)} = \eta_{(0)} + \eta_{tide} \tag{C.2}$$

$$\vec{U}_{(3)} = \frac{H+\eta_{(0)}}{H+\eta_{(1)}}\vec{U}_{(2)} + \begin{cases} \frac{H}{H+\eta_{(1)}}\vec{U}_{tide} & \text{linear tidal model} \\ \frac{H+\eta_{tide}}{H+\eta_{(1)}}\vec{U}_{tide} & \text{nonlinear tidal model} \end{cases} \tag{C.3}$$

Finally these elevations and transports are combined with the chosen vertical shear and continuity to obtain the initial velocities:

$$\vec{u}' = \begin{cases} \vec{u}_{(2)} - \frac{1}{H+\eta_{(1)}}\int_{-H}^{\eta_{(1)}}\vec{u}_{(2)}\,dz & \text{if 3D constraints (see Appendix B)} \\ \vec{u}_{(1)} - \frac{1}{H+\eta_{(1)}}\int_{-H}^{\eta_{(1)}}\vec{u}_{(1)}\,dz & \text{otherwise} \end{cases} \tag{C.4}$$

$$\vec{u} = \vec{u}' + \vec{U}_{(3)} \tag{C.5}$$

$$w = -\int_{-H}^{z}\nabla\cdot\vec{u}\,d\zeta - (\vec{u}\cdot\nabla H)\big|_{z=-H} \tag{C.6}$$

With these choices for $\vec{u}$ and w, the initial velocities will also satisfy

$$w\big|_{z=\eta_{(1)}} = \frac{\partial\eta_{tide}}{\partial t} + \left(\vec{u}\cdot\nabla\eta_{(1)}\right)\Big|_{z=\eta_{(1)}}; \quad w\big|_{z=-H} = -(\vec{u}\cdot\nabla H)\big|_{z=-H};$$
$$\frac{\partial\eta_{tide}}{\partial t} + \nabla\cdot\int_{-H}^{\eta_{(1)}}\vec{u}\,dz = 0$$

which represent the kinematic BCs at the top and bottom and the vertically integrated conservation of mass, all under the previously stated assumption that non-tidal temporal variations in the free surface are negligible. Note that for time-dependent BCs, the superposition of tidal and sub tidal components is also done, but with the sub-tidal components computed above and the tidal components evaluated in real time from an attached tidal model.

Appendix D. Derivations of cost functions

Here we briefly outline the derivation the cost functions and subsequent schemes for optimizing them. Details are in available in Haley et al. (2014).

D.1. Evaluating full domain cost function, J, for variations around Ψ

Substituting Eq. (3) or Eq. (4) in Eq. (2), and performing a bit of algebra to transfer the $\hat{k}\times$ term, we obtain for J,

$$J(\widetilde{\Psi}) = \frac{1}{2}\iint_{\mathcal{D}}\omega\left(\hat{k}\times H\vec{U}_{(0)} + \nabla\widetilde{\Psi}\right)\cdot\left(\hat{k}\times H\vec{U}_{(0)} + \nabla\widetilde{\Psi}\right)da. \tag{D.1}$$

Applying calculus of variations to obtain the Ψ that minimizes J yields

$$J(\Psi+\delta\Psi) = J(\Psi) + \frac{1}{2}\iint_{\mathcal{D}} \omega\|\nabla(\delta\Psi)\|^2\, da - \iint_{\mathcal{D}} \delta\Psi\nabla\cdot\left[\omega\left(\nabla\Psi + \hat{k}\times H\vec{U}_{(0)}\right)\right] da + \oint_{\partial\mathcal{D}} \omega\delta\Psi\left(\nabla\Psi + \hat{k}\times H\vec{U}_{(0)}\right)\cdot\hat{n}\, ds \quad \text{(D.2)}$$

where $\partial\mathcal{D}$ is the boundary of the domain $\mathcal{D}$. Ψ will minimize J provided the second and third integrals in Eq. (D.2) are zero for all permissible choices of $\delta\Psi$. The second integral will only be identically zero for all $\delta\Psi$ if the divergence in the integrand is everywhere zero. For the third integral around $\partial\mathcal{D}$, two choices exist. One choice would be to set $(\nabla\Psi + \hat{k}\times H\vec{U}_{(0)})\cdot\hat{n}$ to zero along $\partial\mathcal{D}$. This condition would constrain the circulation around the domain. The other choice is to provide Dirichlet BCs to the problem for $\widetilde{\Psi}$, which, in turn, limits the variations $\delta\Psi$ to those that vanish along the boundary ($\delta\Psi|_{\partial\mathcal{D}} = 0$). Dirichlet BCs provide a pathway for incorporating information on the transports into and out of the domain. Such information is an important addition to reduced physics initializations (e.g. geostrophy), providing constraints on the external forcing applied to the domain. To summarize, the second integrand is set to zero along with Dirichlet BCs.

D.2. Evaluating exterior boundary cost function, J_{b^e}, for variations around Ψ_{b^e}

We separate Eq. (6) into a series of integrals along the open boundaries and a series of integrals along the coasts. We introduce the set of M^e labels for the M^e external coasts $\{C^{\mathrm{e}}_m\}$. The corresponding set of M^e open boundary segments go from one external coast to the next. They are defined such that the m^{th} open boundary segment starts at external coast C^{e}_m and ends at external coast C^{e}_{m+1} or C^{e}_1 if $m = M^e$. To denote this, we use the notation $C^{\mathrm{e}}_{\widetilde{m}}$. J_{b^e} is then rewritten in terms of the open and coastal contributions:

$$J_{b^e}(\widetilde{\Psi}_{b^e}) = \frac{1}{2}\sum_{m=1}^{M^e}\int_{C^{\mathrm{e}+}_m}^{C^{\mathrm{e}-}_{\widetilde{m}}} \omega\left(\frac{\partial\widetilde{\Psi}_{b^e}}{\partial s} + H\vec{U}_{(0)}\cdot\hat{n}\right)^2 ds + \frac{1}{2}\sum_{m=1}^{M^e}\int_{C^{\mathrm{e}}_m}\omega\left(H\vec{U}_{(0)}\cdot\hat{n}\right)^2 ds \quad \text{(D.3)}$$

where the $+/-$ notation in $C^{\mathrm{e}+}_m$ were defined just after Eq. (8). The first series of integrals contains the contributions from the open sections of $\partial\mathcal{D}^e$ while the second contains the contributions from the external coasts. Variational calculus results in an equation different from, but similar to, (D.2):

$$J_{b^e}(\Psi_{b^e}+\delta\Psi_{b^e}) = J_{b^e}(\Psi_{b^e}) + \frac{1}{2}\sum_{m=1}^{M^e}\int_{C^{\mathrm{e}+}_m}^{C^{\mathrm{e}-}_{\widetilde{m}}}\omega\left(\frac{\partial\delta\Psi_{b^e}}{\partial s}\right)^2 ds - \sum_{m=1}^{M^e}\int_{C^{\mathrm{e}+}_m}^{C^{\mathrm{e}-}_{\widetilde{m}}}\delta\Psi_{b^e}\frac{\partial}{\partial s}\left[\omega\left(\frac{\partial\Psi_{b^e}}{\partial s} + H\vec{U}_{(0)}\cdot\hat{n}\right)\right] ds - \sum_{m=1}^{M^e}\left[\omega\left(\frac{\partial\Psi_{b^e}}{\partial s} + H\vec{U}_{(0)}\cdot\hat{n}\right)\right]\Bigg|_{C^{\mathrm{e}+}_m}^{C^{\mathrm{e}-}_{\widetilde{m}}}(\delta\Psi_{b^e})|_{C^{\mathrm{e}}_m}. \quad \text{(D.4)}$$

Here the contributions from the external coasts are all contained in $J_{b^e}(\Psi_{b^e})$, leaving only the open boundaries (the 3 series) affected by the variations $\delta\Psi_{b^e}$. Ψ_{b^e} is guaranteed to minimize Eq. (6) if the last

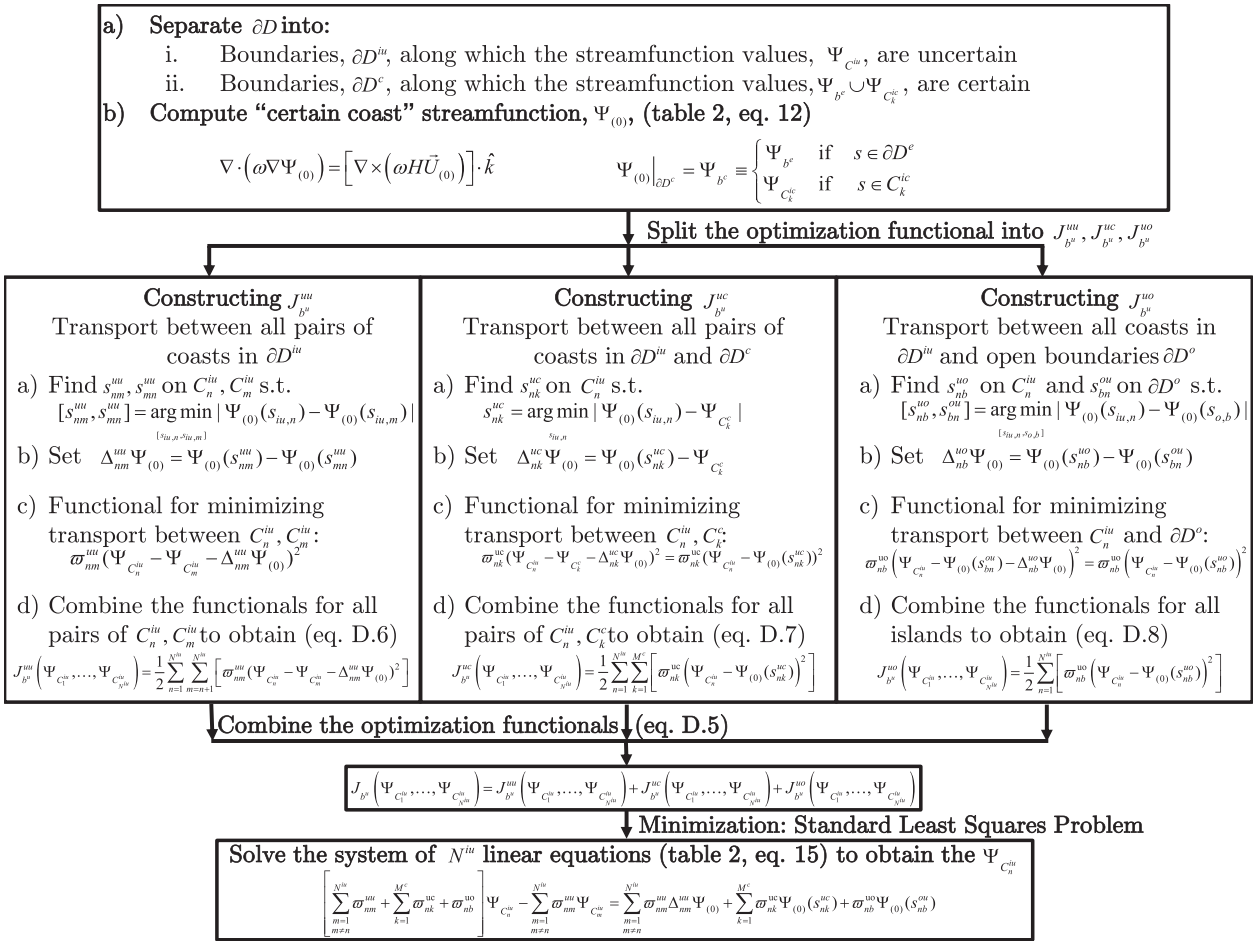

Fig. 13. Flowchart for constructing J_{b^u} and computing streamfunction along uncertain islands $\Psi_{C^{iu}_n}$.

two series in Eq. (D.4) are zero for all permissible $\delta\Psi_{b^e}$, resulting in Eq. (7) and (8).

D.3. Deriving cost function, J_{b^u}, for optimizing Ψ along uncertain coasts, C^{iu}

The optimization functional, J_{b^u}, is constructed as the sum of three terms:

$$J_{b^u}\left(\Psi_{C_1^{\mathrm{iu}}},\ldots,\Psi_{C_{N^{iu}}^{\mathrm{iu}}}\right) = J_{b^u}^{uu}\left(\Psi_{C_1^{\mathrm{iu}}},\ldots,\Psi_{C_{N^{iu}}^{\mathrm{iu}}}\right) + J_{b^u}^{uc}\left(\Psi_{C_1^{\mathrm{iu}}},\ldots,\Psi_{C_{N^{iu}}^{\mathrm{iu}}}\right) + J_{b^u}^{uo}\left(\Psi_{C_1^{\mathrm{iu}}},\ldots,\Psi_{C_{N^{iu}}^{\mathrm{iu}}}\right) \tag{D.5}$$

where $J_{b^u}^{uu}$ is the optimizing functional for the transport between all pairs of the uncertain coasts, $J_{b^u}^{uc}$ is the optimizing functional for the transport between all pairs of uncertain and certain coasts and $J_{b^u}^{uo}$ is the optimizing functional for the transport between each of the uncertain coasts and the open boundaries of the domain (Fig. 13). We introduce the superscript notation *uu* for functionals and quantities evaluated between pairs of uncertain coasts, *uc* between uncertain and certain coasts and *uo* between uncertain coasts and the open boundaries. The three terms in Eq. (D.5) are constructed as follows:

1. *Constructing $J_{b^u}^{uu}$:* Let C_n^{iu} and C_m^{iu} be two of the coasts in $\partial\mathcal{D}^{iu}$. $\Psi_{(0)}$ is not constrained to be a constant along these coasts. Denoting a point s on C_m^{iu} by $s_{iu,m}$, we find the points s_{nm}^{uu} and s_{mn}^{uu} which minimize the transport (as estimated by $\Psi_{(0)}$) between the islands:

$$[s_{nm}^{uu}, s_{mn}^{uu}] = \underset{[s_{iu,n}, s_{iu,m}]}{\arg\min} \mid \Psi_{(0)}(s_{iu,n}) - \Psi_{(0)}(s_{iu,m}) \mid$$

(i.e. s_{nm}^{uu} is the point along C_n^{iu} which minimizes the difference in $\Psi_{(0)}$ between C_n^{iu} and C_m^{iu}). Then, denoting $\Delta_{nm}^{uu}\Psi_{(0)} = \Psi_{(0)}(s_{nm}^{uu}) - \Psi_{(0)}(s_{mn}^{uu})$, the optimization functional for the transport between islands n and m is chosen to be $\varpi_{nm}^{\mathrm{uu}}(\Psi_{C_n^{\mathrm{iu}}} - \Psi_{C_m^{\mathrm{iu}}} - \Delta_{nm}^{uu}\Psi_{(0)})^2$ where $\Psi_{C_n^{\mathrm{iu}}}$, $\Psi_{C_m^{\mathrm{iu}}}$ are the unknown optimized (constant) values of the transport streamfunction along coasts n and m respectively. $\varpi_{nm}^{\mathrm{uu}}$ is a weight applied to the inter-island transport difference in the optimization. The weights are chosen to emphasize the transports between adjacent islands over the transports between widely separated islands (e.g. in Fig. 1, the transport between islands 2 and 3 will be much more heavily weighted than the transport between islands 1 and 3). The details of the weighting function are presented in Section 3.2.1. Summing these weighted differences over all distinct pairs of islands (and pre-multiplying by $\frac{1}{2}$) results in:

$$J_{b^u}^{uu}\left(\Psi_{C_1^{\mathrm{iu}}},\ldots,\Psi_{C_{N^{iu}}^{\mathrm{iu}}}\right) = \frac{1}{2}\sum_{n=1}^{N^{iu}}\sum_{m=n+1}^{N^{iu}}\left[\varpi_{nm}^{\mathrm{uu}}\left(\Psi_{C_n^{\mathrm{iu}}} - \Psi_{C_m^{\mathrm{iu}}} - \Delta_{nm}^{uu}\Psi_{(0)}\right)^2\right] \tag{D.6}$$

2. *Constructing $J_{b^u}^{uc}$:* Let C_k^{c} be one of the coasts in $\partial\mathcal{D}^{c}$, $\Psi_{C_k^{\mathrm{c}}}$ be the certain (constant) value of Ψ along C_k^{c} and C_n^{iu} be a coast in $\partial\mathcal{D}^{iu}$. Find the point s_{nk}^{uc} on C_n^{iu} which minimizes the transport (as estimated by $\Psi_{(0)}$) between the island and certain coast:

$$s_{nk}^{uc} = \underset{s_{iu,n}}{\arg\min} \mid \Psi_{(0)}(s_{iu,n}) - \Psi_{C_k^{\mathrm{c}}} \mid$$

and define $\Delta_{nk}^{uc}\Psi_{(0)} = \Psi_{(0)}(s_{nk}^{uc}) - \Psi_{C_k^{\mathrm{c}}}$. The optimization functional for the transport between island n and coast k is chosen to be $\varpi_{nk}^{\mathrm{uc}}(\Psi_{C_n^{\mathrm{iu}}} - \Psi_{C_k^{\mathrm{c}}} - \Delta_{nk}^{uc}\Psi_{(0)})^2 = \varpi_{nk}^{\mathrm{uc}}(\Psi_{C_n^{\mathrm{iu}}} - \Psi_{(0)}(s_{nk}^{uc}))^2$. Here the certain value $\Psi_{C_k^{\mathrm{c}}}$ cancels out. One side effect of this cancellation is that this functional provides a mechanism for the constant of integration selected in constructing Ψ_b to enter into the optimization (while $J_{b^u}^{uu}$ retains only differences of $\Psi_{(0)}$). As before, the transport differences are weighted by $\varpi_{nk}^{\mathrm{uc}}$. Summing these weighted differences over all pairs of islands and coasts (and pre-multiplying by $\frac{1}{2}$) results in:

$$J_{b^u}^{uc}\left(\Psi_{C_1^{\mathrm{iu}}},\ldots,\Psi_{C_{N^{iu}}^{\mathrm{iu}}}\right) = \frac{1}{2}\sum_{n=1}^{N^{iu}}\sum_{k=1}^{M^{c}}\left[\varpi_{nk}^{\mathrm{uc}}\left(\Psi_{C_n^{\mathrm{iu}}} - \Psi_{(0)}(s_{nk}^{uc})\right)^2\right] \tag{D.7}$$

3. *Constructing $J_{b^u}^{uo}$:* Let $s_{o,b}$ be a point along the open boundary, $\partial\mathcal{D}^{o}$. Find s_{nb}^{uo} on C_n^{iu} and s_{bn}^{ou} on $\partial\mathcal{D}^{o}$ which minimizes the transport (as estimated by $\Psi_{(0)}$) between the island and open boundary:

$$[s_{nb}^{uo}, s_{bn}^{ou}] = \underset{[s_{iu,n}, s_{o,b}]}{\arg\min} \mid \Psi_{(0)}(s_{iu,n}) - \Psi_{(0)}(s_{o,b}) \mid$$

Then, defining $\Delta_{nb}^{uo}\Psi_{(0)} = \Psi_{(0)}(s_{nb}^{uo}) - \Psi_{(0)}(s_{bn}^{ou})$, the optimization functional for the transport between the island n and the open boundary is chosen to be $\varpi_{nb}^{\mathrm{uo}}(\Psi_{C_n^{\mathrm{iu}}} - \Psi_{(0)}(s_{bn}^{ou}) - \Delta_{nb}^{uo}\Psi_{(0)})^2 = \varpi_{nb}^{\mathrm{uo}}(\Psi_{C_n^{\mathrm{iu}}} - \Psi_{(0)}(s_{nb}^{uo}))^2$. As above, the transport difference is weighted by $\varpi_{nb}^{\mathrm{uo}}$ and the known value of Ψ along the boundary cancels (providing a second path for information on the constant of integration). Summing these weighted differences over all islands (and pre-multiplying by $\frac{1}{2}$) results in:

$$J_{b^u}^{uo}\left(\Psi_{C_1^{\mathrm{iu}}},\ldots,\Psi_{C_{N^{iu}}^{\mathrm{iu}}}\right) = \frac{1}{2}\sum_{n=1}^{N^{iu}}\left[\varpi_{nb}^{\mathrm{uo}}\left(\Psi_{C_n^{\mathrm{iu}}} - \Psi_{(0)}(s_{nb}^{uo})\right)^2\right] \tag{D.8}$$

These expressions for $J_{b^u}^{uu}$, $J_{b^u}^{uc}$ and $J_{b^u}^{uo}$ are substituted into Eq. (D.5), resulting in Eq. (14). $J_{b^u}^{uc}$ and $J_{b^u}^{uo}$ provide a pathway for the absolute value of Ψ_{b^e} (i.e. the constant of integration) to be included in the optimized $\Psi_{C^{\mathrm{iu}}}$, since they are formulated directly in terms of the $\Psi_{C^{\mathrm{iu}}}$'s. In contrast, the formulation of $J_{b^u}^{uu}$ in terms of differences between the $\Psi_{C^{\mathrm{iu}}}$'s provides the algorithm robustness to non-localized changes from imposing the $\Psi_{C^{\mathrm{iu}}}$ (i.e. the values along C^{iu} are allowed to "float" with the changes).

References

Agarwal, A., Lermusiaux, P.F.J., 2011. Statistical field estimation for complex coastal regions and archipelagos. Ocean Modell. 40 (2), 164–189.

Agarwal, A., 2009. Statistical Field Estimation and Scale Estimation for Complex Coastal Regions and Archipelagos (Master's thesis). Massachusetts Institute of Technology, Department of Mechanical Engineering, Cambridge, Massachusetts.

Antonov, J.I., Locarnini, R.A., Boyer, T.P., Mishonov, A.V., Garcia, H.E., 2006. In: Levitus, S. (Ed.), World Ocean Atlas 2005, Salinity. NOAA Atlas NESDIS 62, vol. 2. US Government Printing Office, Washington, DC.

Artale, V., Calmanti, S., Carillo, A., Dell Aquila, A., Herrmann, M., Pisacane, G., Ruti, P.M., Sannino, G., Struglia, M.V., Giorgi, F., Bi, X., Pal, J.S., Rauscher, S., 2010. An atmosphere-ocean regional climate model for the Mediterranean area: assessment of a present climate simulation. Clim. Dyn. 35 (5), 721–740.

Balmaseda, M., Anderson, D., 2009. Impact of initialization strategies and observations on seasonal forecast skill. Geophys. Res. Lett. 36 (1), L01701.

Balmaseda, M.A., Vidard, A., Anderson, D.L., 2008. The ECMWF ocean analysis system: ORA-S3. Mon. Weather Rev. 136 (8), 3018–3034.

Barth, A., Alvera-Azcrate, A., Weisberg, R.H., 2008. Benefit of nesting a regional model into a large-scale ocean model instead of climatology. Application to the West Florida Shelf. Cont. Shelf Res. 28 (4–5), 561–573.

Bender, M.A., Ginis, I., 2000. Real-case simulations of hurricane–ocean interaction using a high-resolution coupled model: effects on hurricane intensity. Mon. Weather Rev. 128 (4), 917–946.

Bennett, A.F., 1992. Inverse Methods in Physical Oceanography. Cambridge University Press.

Bennett, A.F., 2002. Inverse Modeling of the Ocean and Atmosphere. Cambridge University Press.

Beşiktepe, Ş.T., Lermusiaux, P.F.J., Robinson, A.R., 2003. Coupled physical and biogeochemical data-driven simulations of Massachusetts Bay in late summer: real-time and postcruise data assimilation. J. Mar. Syst. 40–41, 171–212.

Bleck, R., 2002. An oceanic general circulation model framed in hybrid isopycnic-Cartesian coordinates. Ocean Modell. 4 (1), 55–88.

Boyer, T.P., Stephens, C., Antonov, J.I., Conkright, M.E., Locarnini, R.A., O'Brien, T.D., Garcia, H.E., 2002. In: Levitus, S. (Ed.), World Ocean Atlas 2001, Salinity. NOAA Atlas NESDIS 50. US Government Printing Office, Washington, DC.

Cazes-Boezio, G., Menemenlis, D., Mechoso, C.R., 2008. Impact of ECCO ocean-state estimates on the initialization of seasonal climate forecasts. J. Clim. 21 (9), 1929–1947.

Chavanne, C., Flament, P., Gurgel, K.-W., 2007. Observations of vortices and vortex rossby waves in the lee of an island. In: 18th Congres Francais de Mecanique. URL <http://hdl.handle.net/2042/16729>.

Colin, M., Duda, T., te Raa, L., van Zon, T., Haley, P., Lermusiaux, P., Leslie, W., Mirabito, C., Lam, F., Newhall, A., Lin, Y.-T., Lynch, J., 2013. Time-evolving acoustic propagation modeling in a complex ocean environment. In: OCEANS – Bergen, 2013 MTS/IEEE. pp. 1–9.

Cossarini, G., Lermusiaux, P.F.J., Solidoro, C., 2009. The Lagoon of Venice ecosystem: seasonal dynamics and environmental guidance with uncertainty analyses and error subspace data assimilation. J. Geophys. Res. 114, C0626.

Cushman-Roisin, B., Beckers, J.-M., 2010. Introduction to Geophysical Fluid Dynamics: Physical and Numerical Aspects. Academic Press.

Deleersnijder, E., Legat, V., Lermusiaux, P.F.J., 2010. Multi-scale modelling of coastal, shelf and global ocean dynamics. Ocean Dyn. 60 (6), 1357–1359.

Denaro, F.M., 2003. On the application of the Helmholtz–Hodge decomposition in projection methods for incompressible flows with general boundary conditions. Int. J. Numer. Methods Fluids 43 (1), 43–69.

Dijkstra, H.A., Katsman, C.A., 1997. Temporal variability of the wind-driven quasi-geostrophic double gyre ocean circulation: basic bifurcation diagrams. Geophys. Astrophys. Fluid Dyn. 85 (3–4), 195–232.

Egbert, G.D., Erofeeva, S.Y., 2002. Efficient inverse modeling of barotropic ocean tides. J. Atmos. Oceanic Technol. 19 (2), 183–204.

Egbert, G.D., Erofeeva, S.Y., 2013. TPXO8-ATLAS. URL <http://volkov.oce.orst.edu/tides/tpxo8atlas.html>

Falkovich, A., Ginis, I., Lord, S., 2005. Ocean data assimilation and initialization procedure for the coupled GFDL/URI hurricane prediction system. J. Atmos. Oceanic Technol. 22 (12), 1918–1932.

Firing, J., Brainard, R.E., 2004. Ten years of shipboard ADCP measurements along the northwestern Hawaiian Islands. Tech. rep., Third Scientific Symposium, Honolulu.

Gangopadhyay, A., Robinson, A.R., Haley Jr., P.J., Leslie, W.G., Lozano, C.J., Bisagni, J.J., Yu, Z., 2003. Feature oriented regional modeling and simulations (FORMS) in the Gulf of Maine and Georges Bank. Cont. Shelf Res. 23 (3–4), 317–353.

Gangopadhyay, A., Lermusiaux, P.F., Rosenfeld, L., Robinson, A.R., Calado, L., Kim, H.S., Leslie, W.G., Haley Jr., P.J., 2011. The California current system: a multiscale overview and the development of a feature-oriented regional modeling system (FORMS). Dyn. Atmos. Oceans 52 (1–2), 131–169, special issue of DAO in honor of Prof. A.R.Robinson.

Gangopadhyay, A., Schmidt, A., Agel, L., Schofield, O., Clark, J., 2013. Multiscale forecasting in the Western North Atlantic: sensitivity of model forecast skill to glider data assimilation. Cont. Shelf Res. 63, S159–S176.

Gawarkiewicz, G., Jan, S., Lermusiaux, P.F.J., McClean, J.L., Centurioni, L., Taylor, K., Cornuelle, B., Duda, T.F., Wang, J., Yang, Y.J., Sanford, T., Lien, R.-C., Lee, C., Lee, M.-A., Leslie, W., Haley Jr., P.J., Niiler, P.P., Gopalakrishnan, G., Velez-Belchi, P., Lee, D.-K., Kim, Y.Y., 2011. Circulation and intrusions northeast of Taiwan: chasing and predicting uncertainty in the cold dome. Oceanography 24 (4), 110–121.

Godfrey, J.S., 1989. A Sverdrup model of the depth-integrated flow for the world ocean allowing for island circulations. Geophys. Astrophys. Fluid Dyn. 45 (1–2), 89–112.

Gordon, A.L., Villanoy, C.L., 2011. Oceanography. Special issue on the Philippine Straits Dynamics Experiment. Vol. 24. The Oceanography Society.

Gordon, A.L., Sprintall, J., Ffield, A., 2011. Regional oceanography of the Philippine Archipelago. Oceanography 24 (1), 15–27.

Haley Jr., P.J., Lermusiaux, P.F.J., 2010. Multiscale two-way embedding schemes for free-surface primitive equations in the multidisciplinary simulation, estimation and assimilation system. Ocean Dyn. 60 (6), 1497–1537.

Haley Jr., P.J., Lermusiaux, P.F.J., Robinson, A.R., Leslie, W.G., Logoutov, O., Cossarini, G., Liang, X.S., Moreno, P., Ramp, S.R., Doyle, J.D., Bellingham, J., Chavez, F., Johnston, S., 2009. Forecasting and reanalysis in the Monterey Bay/California current region for the autonomous ocean sampling network-II experiment. Deep Sea Res. II 56 (3–5), 127–148.

Haley, Jr., P.J., Agarwal, A., Lermusiaux, P.F.J., 2014. Deriving a methodology for optimizing velocities and transports in complex coastal regions and archipelagos. MSEAS Report 19, Massachusetts Institute of Technology, Cambridge, MA, USA.

Halliwell Jr., G.R., Shay, L.K., Jacob, S.D., Smedstad, O.M., Uhlhorn, E.W., 2008. Improving ocean model initialization for coupled tropical cyclone forecast models using GODAE nowcasts. Mon. Weather Rev. 136 (7), 2576–2591.

Halliwell Jr., G.R., Shay, L.K., Brewster, J.K., Teague, W.J., 2011. Evaluation and sensitivity analysis of an ocean model response to hurricane Ivan. Mon. Weather Rev. 139 (3), 921–945.

Herzfeld, M., Andrewartha, J.R., 2012. A simple, stable and accurate Dirichlet open boundary condition for ocean model downscaling. Ocean Modell. 43–44, 1–21.

Hurlburt, H.E., Metzger, E.J., Sprintall, J., Riedlinger, S.N., Arnone, R.A., Shinoda, T., Xu, X., 2011. Circulation in the Philippine Archipelago simulated by 1/12° and 1/25° global HYCOM and EAS NCOM. Oceanography 24 (1), 28–47.

Jiang, X., Zhong, Z., Jiang, J., 2009. Upper ocean response of the South China Sea to typhoon Krovanh (2003). Dyn. Atmos. Oceans 47 (1), 165–175.

Leben, R.R., Born, G.H., Engebreth, B.R., 2002. Operational altimeter data processing for mesoscale monitoring. Mar. Geod. 25 (1–2), 3–18.

Lermusiaux, P.F.J., 2006. Uncertainty estimation and prediction for interdisciplinary ocean dynamics. J. Comput. Phys. 217 (1), 176–199.

Lermusiaux, P.F.J., 2007. Adaptive modeling, adaptive data assimilation and adaptive sampling. Phys. D: Nonlinear Phen. 230 (1), 172–196.

Lermusiaux, P.F.J., Haley Jr, P.J., Yilmaz, N.K., 2007. Environmental prediction, path planning and adaptive sampling-sensing and modeling for efficient ocean monitoring, management and pollution control. Sea Technol. 48 (9), 35–38.

Lermusiaux, P.F.J., Haley, P.J., Leslie, W.G., Agarwal, A., Logutov, O., Burton, L., 2011. Multiscale physical and biological dynamics in the Philippines Archipelago: predictions and processes. Oceanography 24 (1), 70–89.

Lermusiaux, P.F.J., Schröter, J., Danilov, S., Iskandarani, M., Pinardi, N., Westerink, J.J., 2013. Multiscale modeling of coastal, shelf, and global ocean dynamics. Ocean Dyn. 63 (11–12), 1341–1344.

Lermusiaux, P.F.J., Lolla, T., Haley, P.J., Yigit, K., Ueckermann, M.P., Sondergaard, T., Leslie, W.G., 2015. Science of autonomy: time-optimal path planning and adaptive sampling for swarms of ocean vehicles. In: Curtin, T. (Ed.), Springer Handbook of Ocean Engineering: Autonomous Ocean Vehicles, Subsystems and Control. Springer-Verlag, in press (Ch. 11).

Leslie, W.G., Robinson, A.R., Haley, P., Logoutov, O., Moreno, P., Lermusiaux, P.F.J., Coehlo, E., 2008. Verification and training of real-time forecasting of multi-scale ocean dynamics for maritime rapid environmental assessment. J. Mar. Syst. 69 (1–2), 3–16.

Li, Z., Chao, Y., McWilliams, J.C., 2006. Computation of the streamfunction and velocity potential for limited and irregular domains. Mon. Weather Rev. 134 (11), 3384–3394.

Locarnini, R.A., Mishonov, A.V., Antonov, J.I., Boyer, T.P., Garcia, H.E., 2006. In: Levitus, S. (Ed.), World Ocean Atlas 2005, Temperature. NOAA Atlas NESDIS 61, vol. 1. US Government Printing Office, Washington, DC.

Logutov, O.G., 2008. A multigrid methodology for assimilation of measurements into regional tidal models. Ocean Dyn. 58 (5–6), 441–460.

Logutov, O.G., Lermusiaux, P.F.J., 2008. Inverse barotropic tidal estimation for regional ocean applications. Ocean Modell. 25 (1–2), 17–34.

Lolla, T., Ueckermann, M.P., Yiğit, K., Haley, P.J., Lermusiaux, P.F.J., 2012. Path planning in time dependent flow fields using level set methods. In: IEEE International Conference on Robotics and Automation (ICRA), pp. 166–173.

Lolla, T., Haley Jr., P.J., Lermusiaux, P.F.J., 2014a. Time-optimal path planning in dynamic flows using level set equations: realistic applications. Ocean Dyn. 64 (10), 1399–1417.

Lolla, T., Lermusiaux, P.F.J., Ueckermann, M.P., Haley Jr., P.J., 2014b. Time-optimal path planning in dynamic flows using level set equations: theory and schemes. Ocean Dyn. 64 (10), 1373–1397.

Lorenz, E.N., 1963. Deterministic nonperiodic flow. J. Atmos. Sci. 20 (2), 130–141.

Lozano, C.J., Robinson, A.R., Arango, H.G., Gangopadhyay, A., Sloan, Q., Haley, P.J., Anderson, L., Leslie, W., 1996. An interdisciplinary ocean prediction system: Assimilation strategies and structured data models. In: Malanotte-Rizzoli, P. (Ed.), Modern Approaches to Data Assimilation in Ocean Modeling, Elsevier Oceanography Series, vol. 61. Elsevier, pp. 413–452.

Lozier, M.S., Owens, W.B., Curry, R.G., 1995. The climatology of the North Atlantic. Prog. Oceanogr. 36 (1), 1–44.

Lynch, P., 1989. Partitioning the wind in a limited domain. Mon. Weather Rev. 117 (7), 1492–1500.

Marshall, J., Plumb, R.A., 2008. Atmosphere, Ocean and Climate Dynamics: An Introductory Text. Elsevier Academic Press, London, United Kingdom.

Maslowski, W., Marble, D., Walczowski, W., Schauer, U., Clement, J.L., Semtner, A.J., 2004. On climatological mass, heat, and salt transports through the Barents Sea and Fram Strait from a pan-Arctic coupled ice-ocean model simulation. J. Geophys. Res.: Oceans 109 (C3), C03032.

Mason, E., Molemaker, J., Shchepetkin, A.F., Colas, F., McWilliams, J.C., Sangrà, P., 2010. Procedures for offline grid nesting in regional ocean models. Ocean Modell. 35 (1–2), 1–15.

May, P.W., Doyle, J.D., Pullen, J.D., David, L.T., 2011. Two-way coupled atmosphere-ocean modeling of the PhilEx intensive observational periods. Oceanography 24 (1), 48–57.

Moore, A.M., 1991. Data assimilation in a quasi-geostrophic open-ocean model of the Gulf Stream region using the adjoint method. J. Phys. Oceanogr. 21 (3), 398–427.

Moore, A.M., Arango, H.G., Di Lorenzo, E., Cornuelle, B.D., Miller, A.J., Neilson, D.J., 2004. A comprehensive ocean prediction and analysis system based on the tangent linear and adjoint of a regional ocean model. Ocean Modell. 7 (1), 227–258.

Moore, A.M., Arango, H.G., Broquet, G., Powell, B.S., Weaver, A.T., Zavala-Garay, J., 2011. The regional ocean modeling system (roms) 4-dimensional variational data assimilation systems: Part I – System overview and formulation. Prog. Oceanogr. 91 (1), 34–49.

MSEASgroup, 2010. MSEAS manual. MSEAS Report 6, Massachusetts Institute of Technology, Cambridge, MA, USA.

Oke, P.R., Allen, J.S., Miller, R.N., Egbert, G.D., Kosro, P.M., 2002. Assimilation of surface velocity data into a primitive equation coastal ocean model. J. Geophys. Res.: Oceans 107 (C9), 5-1–5-25.

Onken, R., Álvarez, A., Fernández, V., Vizoso, G., Basterretxea, G., Tintoré, J., Haley Jr., P., Nacini, E., 2008. A forecast experiment in the Balearic Sea. J. Mar. Syst. 71 (1–2), 79–98.

Phadnis, A., 2013. Uncertainty quantification and prediction for non-autonomous linear and nonlinear systems. Master's thesis, Massachusetts Institute of Technology, Cambridge, MA.

Pinardi, N., Allen, I., Demirov, E., Mey, P.D., Korres, G., Lascaratos, A., Traon, P.-Y.L., Maillard, C., Manzella, G., Tziavos, C., 2003. The Mediterranean ocean forecasting system: first phase of implementation (1998–2001). Ann. Geophys. 21 (1), 3–20.

Qiu, B., Koh, D.A., Lumpkin, C., Flament, P., 1997. Existence and formation mechanism of the North Hawaiian ridge current. J. Phys. Oceanogr. 27 (3), 431–444.

Ramp, S., Lermusiaux, P.F.J., Shulman, I., Chao, Y., Wolf, R.E., Bahr, F.L., 2011. Oceanographic and atmospheric conditions on the continental shelf north of the Monterey Bay during August 2006. Dyn. Atmos. Oceans 52 (1–2), 192–223.

Robinson, A., 1996. Physical processes, field estimation and an approach to interdisciplinary ocean modeling. Earth-Sci. Rev. 40 (1–2), 3–54.

Robinson, A.R., 1999. Forecasting and simulating coastal ocean processes and variabilities with the Harvard ocean prediction system. In: Mooers, C.N.K. (Ed.), Coastal Ocean Prediction, Coastal and Estuarine Studies, vol. 56. American Geophysical Union, Washington, DC, pp. 77–99.

Sandery, P.A., Brassington, G.B., Freeman, J., 2011. Adaptive nonlinear dynamical initialization. J. Geophys. Res.: Oceans (1978–2012) 116 (1), C01021.

Sapsis, T.P., Lermusiaux, P.F.J., 2009. Dynamically orthogonal field equations for continuous stochastic dynamical systems. Physica D 238 (23–24), 2347–2360.

Sapsis, T.P., Lermusiaux, P.F.J., 2012. Dynamical criteria for the evolution of the stochastic dimensionality in flows with uncertainty. Physica D 241 (1), 60–76.

Sapsis, T.P., Ueckermann, M.P., Lermusiaux, P.F.J., 2013. Global analysis of Navier–Stokes and Boussinesq stochastic flows using dynamical orthogonality. J. Fluid Mech. 734, 83–113.

Schiller, A., Oke, P.R., Brassington, G., Entel, M., Fiedler, R., Griffin, D.A., Mansbridge, J., 2008. Eddy-resolving ocean circulation in the Asian-Australian region inferred from an ocean reanalysis effort. Prog. Oceanogr. 76 (3), 334–365.

Schmidt, A., Gangopadhyay, A., 2013. An operational ocean circulation prediction system for the western North Atlantic: hindcasting during July–September of 2006. Cont. Shelf Res. 63, S177–S192.

Sethian, J.A., 1996. A fast marching level set method for monotonically advancing fronts. Proc. Natl. Acad. Sci. 93 (4), 1591–1595.

Sethian, J.A., 1999. Level Set Methods and Fast Marching Method. Cambridge University Press, Cambridge, United Kingdom.

Simonnet, E., Dijkstra, H.A., Ghil, M., 2009. Bifurcation analysis of ocean, atmosphere, and climate models. In: Temam, R., Tribbia, J., Ciarlet, P.G. (Eds.), Computational Methods for the Ocean and the Atmosphere, Handbook of Numerical Analysis. Elsevier, pp. 187–229.

Sondergaard, T., Lermusiaux, P.F.J., 2013a. Data assimilation with Gaussian mixture models using the dynamically orthogonal field equations. Part I: Theory and scheme. Mon. Weather Rev. 141 (6), 1737–1760.

Sondergaard, T., Lermusiaux, P.F.J., 2013b. Data assimilation with Gaussian mixture models using the dynamically orthogonal field equations. Part II: Applications. Mon. Weather Rev. 141 (6), 1761–1785.

Stephens, C., Antonov, J.I., Boyer, T.P., Conkright, M.E., Locarnini, R.A., O'Brien, T.D., Garcia, H.E., 2002. In: Levitus, S. (Ed.), World Ocean Atlas 2001, Temperature. NOAA Atlas NESDIS 49, vol. 1. US Government Printing Office, Washington, DC.

Timmermann, R., Goosse, H., Madec, G., Fichefet, T., Ethe, C., Duliere, V., 2005. On the representation of high latitude processes in the ORCA-LIM global coupled sea ice–ocean model. Ocean Modell. 8 (1), 175–201.

Ueckermann, M.P., Lermusiaux, P.F.J., 2010. High order schemes for 2D unsteady biogeochemical ocean models. Ocean Dyn. 60 (6), 1415–1445.

Ueckermann, M.P., Lermusiaux, P.F.J., Sapsis, T.P., 2013. Numerical schemes for dynamically orthogonal equations of stochastic fluid and ocean flows. J. Comput. Phys. 233, 272–294.

Ueckermann, M.P., Lermusiaux, P.F.J., 2015. Hybridizable discontinuous Galerkin projection methods for Navier-Stokes equations. J. Comput. Phys., submitted for publication.

Wunsch, C., 1996. The Ocean Circulation Inverse Problem. Cambridge University Press, Cambridge, United Kingdom.

Xu, J., Lermusiaux, P.F.J., Haley, P.J., Leslie, W.G., Logoutov, O.G., 2008. Spatial and temporal variations in acoustic propagation during the PLUSNet07 exercise in Dabob Bay. In: Proceedings of Meetings on Acoustics (POMA), 155th Meeting Acoustical Society of America 4, p. 070001.

Yablonsky, R.M., Ginis, I., 2008. Improving the ocean initialization of coupled hurricane–ocean models using feature-based data assimilation. Mon. Weather Rev. 136 (7), 2592–2607.

Zhang, J., Steele, M., 2007. Effect of vertical mixing on the Atlantic water layer circulation in the Arctic Ocean. J. Geophys. Res.: Oceans (1978–2012) 112 (4).